Accuracy Improvement for Measurement of Gas Diffusivity through Thin Porous Media

by

Lu Dong

A thesis
presented to the University of Waterloo
in fulfilment of the
thesis requirement for the degree of
Master of Applied Science
in
Mechanical Engineering

Waterloo, Ontario, Canada, 2012

Lu Dong

Abstract

Accurate measurement of the gas diffusion coefficient through porous media is of significant interest to science and engineering applications including mass transfer through soils, building materials, and fuel cells to name a few. Accurate measurements are necessary for simulation and optimization of complex systems involving gas transport. The Loschmidt cell, or closed tube method has been extensively used to measuring the binary gas diffusion coefficient of gas pairs. Recent studies have used a modified Loschmidt cell with an additional porous sample to measure the effective diffusion coefficient through the porous sample. The method employs what is called the resistance network method for calculating the effective diffusion coefficient through the porous sample.

In this study, a one-dimensional simulation was developed to evaluate the accuracy of the resistance network method with a modified Loschmidt cell. Dimensionless parameters are shown to be applicable for both the conventional Loschmidt cell as well as the modified Loschmidt cell with the porous sample. A parametric simulation study was performed to show that the error relates closely to the ratio of diffusive resistances of the sample and bulk gas denoted as the resistance ratio, Ω^*. With a simulated experimental duration of $250s$, which is typical of experiments in literature, the error was found to be negligible when $\Omega^* < 0.1$ but increased dramatically for $\Omega^* > 0.1$ up to a maximum of approximately 20% error. The equivalent Fourier number, $\mathrm{Fo}_{\mathrm{eq}}$, based on the equivalent diffusivity, D_{eq}, was proposed as an approximate expression for the degree to which the concentration gradient in the test cell has evolved. It was found that the error has nearly a linear relationship with $\mathrm{Fo}_{\mathrm{eq}}$. Since a lower $\mathrm{Fo}_{\mathrm{eq}}$ means a less decayed profile with significant transience remaining, as $\mathrm{Fo}_{\mathrm{eq}}$ drops, the the error increases. By controlling the simulation test length for different thickness and diffusivity samples such that $\mathrm{Fo}_{\mathrm{eq}} = 12.5$, the error was reduced to less than 1% over most of the range of parameters and less than 6% over the full range of parameters spanning two orders of magnitude for both thickness and diffusivity.

The resistance network method requires the measurement of the sample thickness, a diffusion length, and two diffusion coefficients using with the modified Loschmidt cell (one with the porous sample and one without). Analysis found that the equation used for calculating the effective diffusion coefficient, D_{eff}, through the porous sample inherently magnifies the relative uncertainty of the measured values in the final calculated value for D_{eff}. When $\Omega^* < 1$, the percentage uncertainty in both diffusion coefficient measurements could potentially be magnified by one or more orders of magnitude. To mitigate uncertainty

in D_{eff}, Ω^* must be greater than 1 to ensure that the uncertainty is magnified by no more than a factor of 2.

This study recommends that modified Loschmidt experiments aim for $\Omega^* = 1$ and $\mathrm{Fo}_{\mathrm{eq}} = 12.5$ to greatly reduce the error and uncertainty in the measurement of D_{eff}.

Acknowledgements

I would like to thank Professor Xianguo Li for his help and guidance throughout the entire process, Grant Unsworth for his help with the physical experiment and being constantly available for discussion on all topics related to diffusion, Carl Chan for the initial set up and work related to the original in-house apparatus, Neil Griffett for his technical expertise in electronics and controls, and family and friends for their continuing support in all my endeavours.

Support from the Natural Sciences and Engineering Research Council (NSERC) of Canada is gratefully acknowledged.

Table of Contents

List of Tables

List of Figures

Chapter 1

Introduction

Polymer electrolyte membrane fuel cells (PEMFC) are a classification of electrochemical energy conversion devices that are currently undergoing extensive research and development in an effort enhance their attractiveness for widespread commercial application. Significant research is directed towards the optimization of fuel cell materials. An important component of the materials related research is the ability to accurately measure material properties.

1.1 Operating Principle of Polymer Electrolyte Membrane Fuel Cells

The PEMFC is an electrochemical device that continuously and directly converts supplied H_2 and O_2 into electrical energy. Additionally, heat and water are products of the reaction that must be continuously removed from the reaction sites. PEMFC's are distinguished from other fuel cells by its use of a quasi-solid electrolyte membrane [9]. The major components of a PEMFC are the flow channel, bipolar plate, gas diffusion layer (GDL), catalyst layer (CL), and polymer electrolyte membrane (PEM). Figure 1.1 shows a schematic of the components related to the flow in a PEMFC. The catalyst layer is either deposited onto the membrane or the GDL and sandwiched in place to form the membrane electrode assembly (MEA)[6]. It is inside the MEA where much of the complex gas diffusion, heat conduction, two phase flow in porous media, electron transport, and ion transport occur.

The two components of greatest interest to this investigation are the GDL and CL since those are two porous substances where gas diffusion occurs.

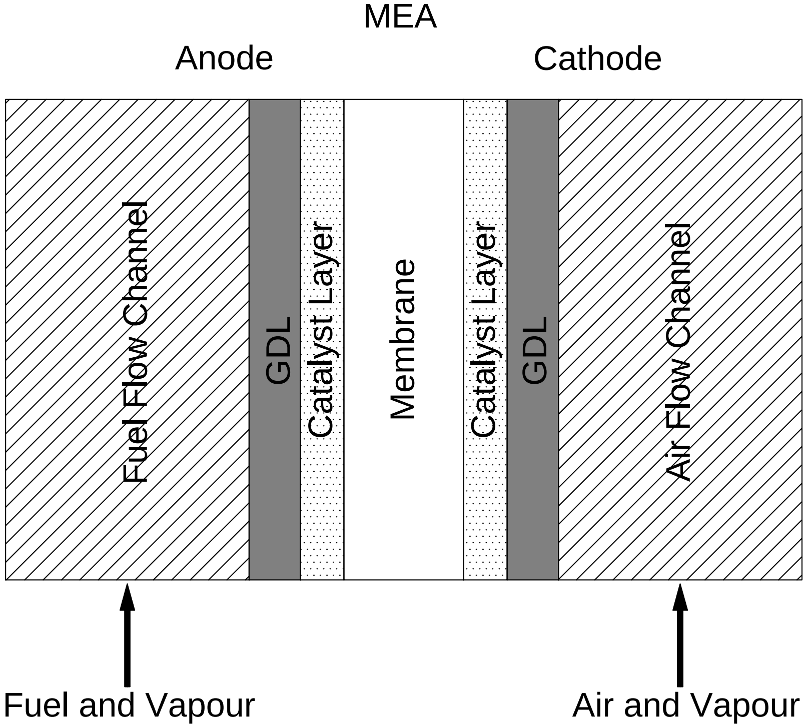

Figure 1.1: Schematic of PEMFC components related to mass flow[1]

During operation, reactant gases are constantly supplied to the flow channels which distribute it over the entire MEA. The reactant gases diffuse through the GDL to the reaction sites within the CL. Figure 1.2 shows a schematic of a single cell as well as the primary processes involved in the reaction. On the anode side, hydrogen is split into an electron and a proton at the reaction site. The electrons flow through the external electrical circuit while the protons move through the membrane. On the cathode side, the oxygen reduction reaction consumes the oxygen and produces water as a product. Water must be transported away from the cathode CL and out through the cathode flow channels.

The most common way of expressing fuel cell performance is through a polarization curve. The curve shows the cell voltage plotted over a range of current densities for a specific set of constant operating conditions. The current density is the total current measured

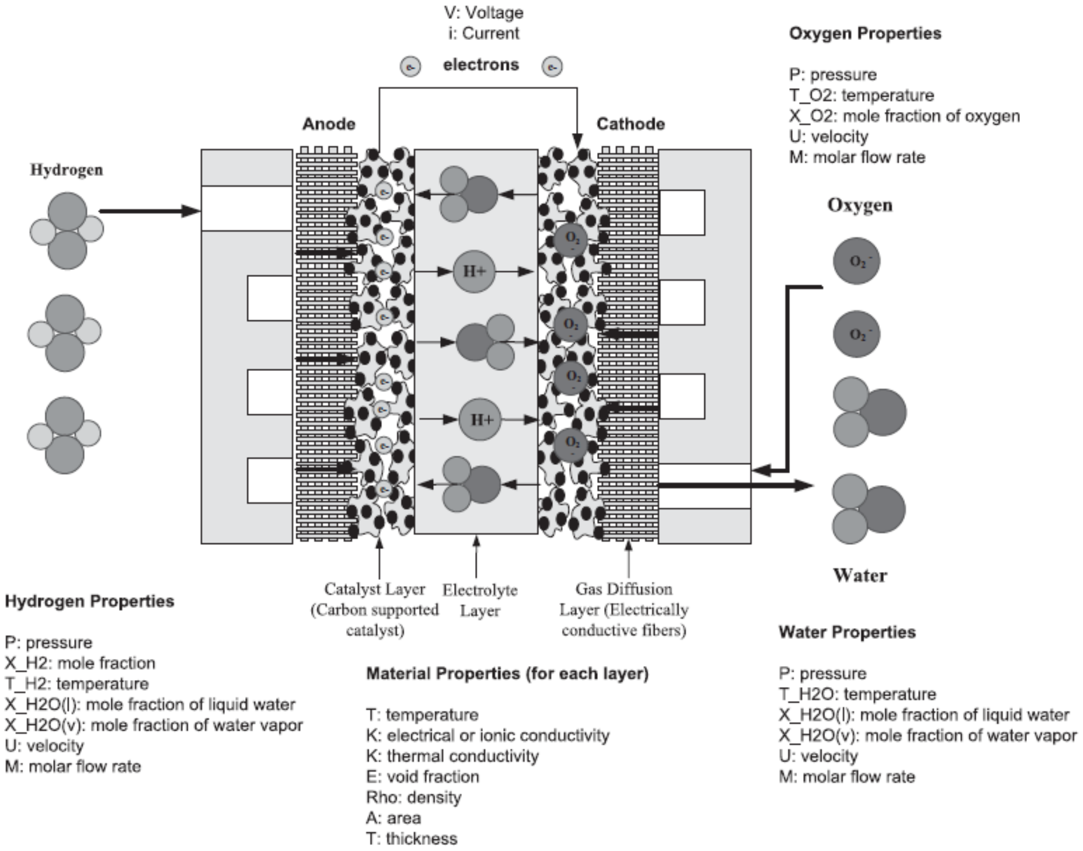

Figure 1.2: Schematic of PEMFC processes during operation [2]

from a running cell divided by the total active area of the fuel cell. Figure 1.3 gives an example of a polarization curve. The loss of voltage observed with increasing current density can be attributed to three types of voltage loss: activation loss (activation polarization), ohmic loss (ohmic polarization), and concentration loss (concentration polarization)[3, 9]. Activation polarization is seen at low current densities and is due in large part to the sluggish kinetics of the oxygen reduction reaction (ORR). Ohmic polarization is caused by the resistance to flow of ions and electrons and is dominant in the intermediate current densities. The ohmic polarization region has a linear profile. The rapid voltage loss in the region of high current density is the concentration polarization. This is due to the drop of concentration of reactants at the reaction site and causes a sharp drop in voltage.

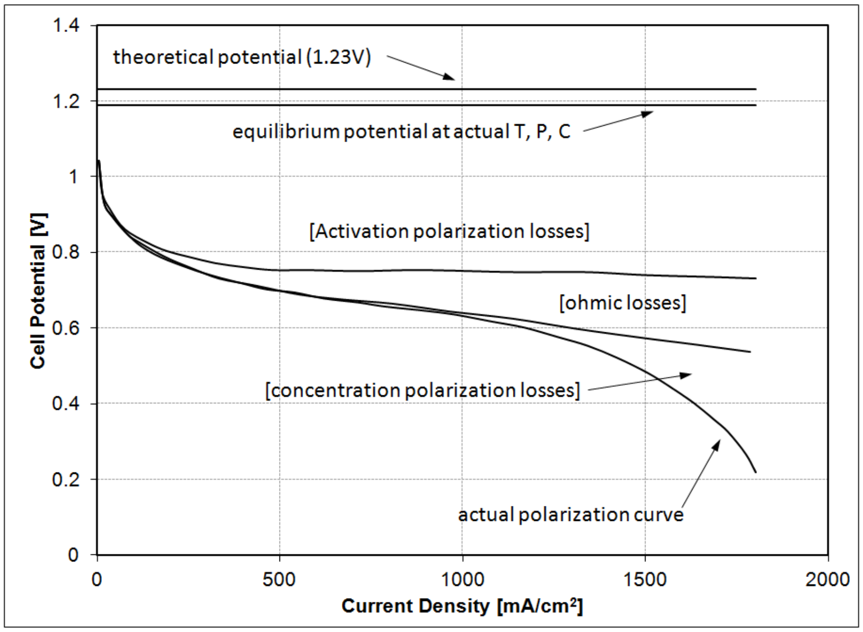

Figure 1.3: Fuel cell voltage losses shown on a polarization curve [3]

The concentration polarization arises due to insufficient transport of reactant gases to the catalyst layer and flooding due to produced water. A significant amount of research deals with water management and two phase flow in fuel cell porous media. The other side of the mass transport limitation is the diffusion of gases in porous media. Knowledge and understanding of gas diffusion performance in fuel cell media is important for the purpose of simulating fuel cell performance, optimizing operating conditions, and design of fuel cell porous media.

1.2 Structure of Porous Diffusion Media in Fuel Cells

The CL and GDL are the porous materials used in PEM fuel cells. the CL contains the reaction sites and is required to transport electrons, ions, and heat in addition to gas and liquid (in the pores). Aside from gas transport, the GDL is used for electron and heat transport. The GDL is also used as mechanical support for the CL. In having these multiple and varied functions, fuel cell porous media have very specific attributes to help it meet these needs.

1.2.1 Gas Diffusion Layer Structure

The GDL is particularly important at high current densities and/or low gas flow rates where blockage by water can potentially dominate voltage losses [10].The ideal GDL serves the purpose of effectively transporting and dispersing reactant gas to the CL while having minimal electrical resistance, create good electrical contact with neighbouring regions, and have appropriate surface wettability to improve water removal [9, 5, 11].

GDL is most commonly a carbon paper made up of planar sheets of randomly oriented carbon fibres. Multiple sheets are stacked to reach the usual thickness of $200\mu m$ to $500\mu m$. While woven carbon cloths are also an alternative, academic and industrial interest centres around carbon paper due to cost advantages and ease of fabricating micro-porous layers (MPL) or CL's directly onto the substrate [4]. In many GDL's additives such as polytetrafluoroethylene (PTFE) or fluorinated ethylene propylene (FEP) are added to make the entire layer more hydrophobic for enhanced water removal. The addition of PTFE has a dramatic effect on the diffusion through the GDL by changing the pore structure and reducing the overall porosity. Figure 1.4 shows the structure of typical GDL with and without hydrophobic treatment.

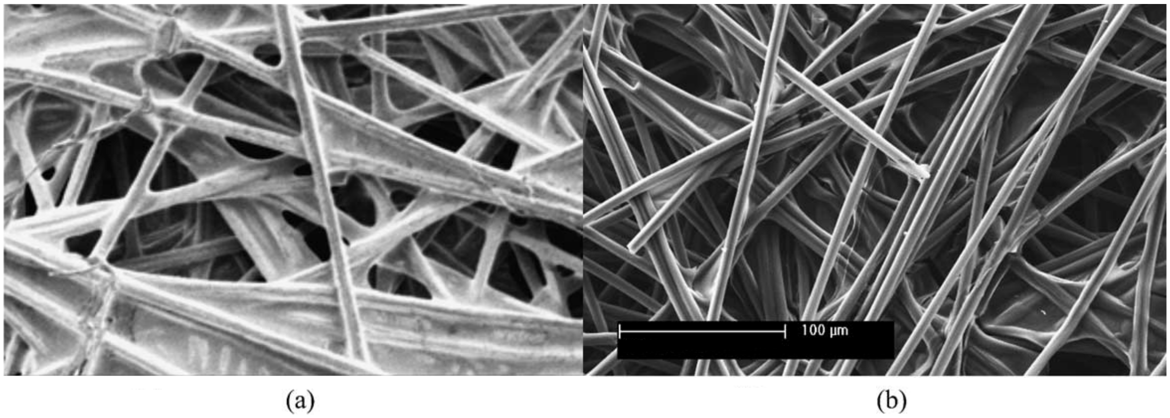

(a) (b)

Figure 1.4: Comparison of surface SEM micrographs of (a) carbon paper impregnated with 20wt.% fluorinated ethylene propylene (FEP) and (b) untreated carbon paper [4]

In some applications, an MPL is added to the side of the GDL in contact with the CL. The MPL is composed of a carbon powder bonded together with PTFE [12]. It serves the purpose of increasing electrical contact with the CL, enhancing water transport away from the reaction site, and preventing intrusion of the CL into the much larger pores of the GDL [4, 13, 11]. Figure 1.5 shows a CL, MPL, and GDL layer as well as their approximate thickness. The GDL and MPL combination is commonly referred to as a double-layer.

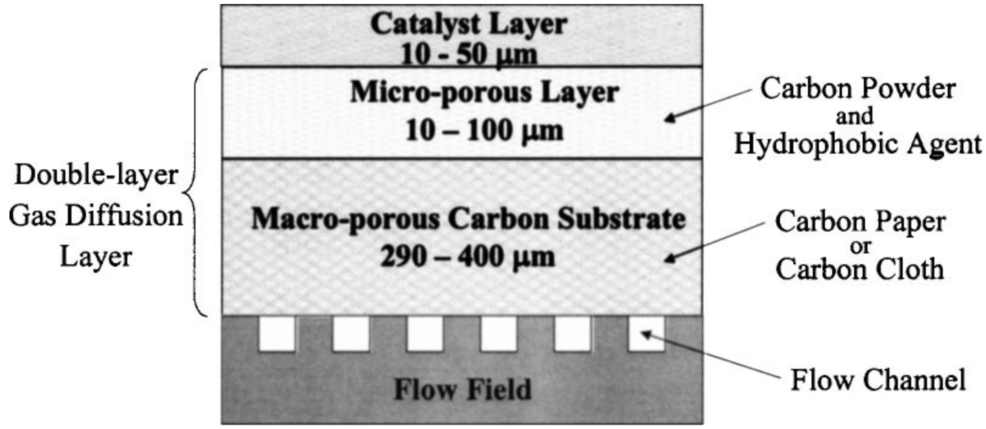

Figure 1.5: Schematic of a double-layer GDL in contact with CL and flow field [5]

A large number of experimental and modelling studies have investigated the effect of GDL and MPL properties on the fuel cell performance [13]. The parameters of porosity, PTFE (or other additive) content, thickness, and MPL properties are all subject to optimization. The accurate measurement of gas diffusion coefficients through these porous structures would provide valuable information for both experimental and simulation studies.

1.2.2 Catalyst Layer Structure

Catalyst layers (CL) in the PEMFC are the regions where the two half cell reactions occur. Typically, platinum catalyst is used to accelerate the reaction to a rate acceptable for practical applications. CL's are composed of platinum particles dispersed on a carbon particle support, an ionomer (similar or the same as the membrane material) for ion transport, a binder to hold together the carbon particles, and in some instances a hydrophobic additive to enhance liquid transport. Current commercial and experimental manufacturing methods for the CL include direct casting, decal transfer, screen printing, spraying, ink jet printing, spray pyrolysis, sputter deposition, and vapour film deposition [14, 15, 16, 17, 18, 19, 7, 6, 20]. The primary goals of exploring so many methods of

CL deposition is to optimize structure for increased performance, decrease cost of materials used (primarily platinum), and reduce the cost of manufacturing. For conventional methods, the CL is first prepared as a catalyst ink solution or colloid containing the carbon supported platinum, a binder, and a solvent [21, 18]. The binder may be either the ionomer or a hydrophobic treatment such as PTFE [14, 17]. As shown in Figure 1.6, the CL can be deposited first onto either the GDL or membrane (A-anode and C-cathode). The membrane covered by CL is called a catalyst coated membrane (CCM).

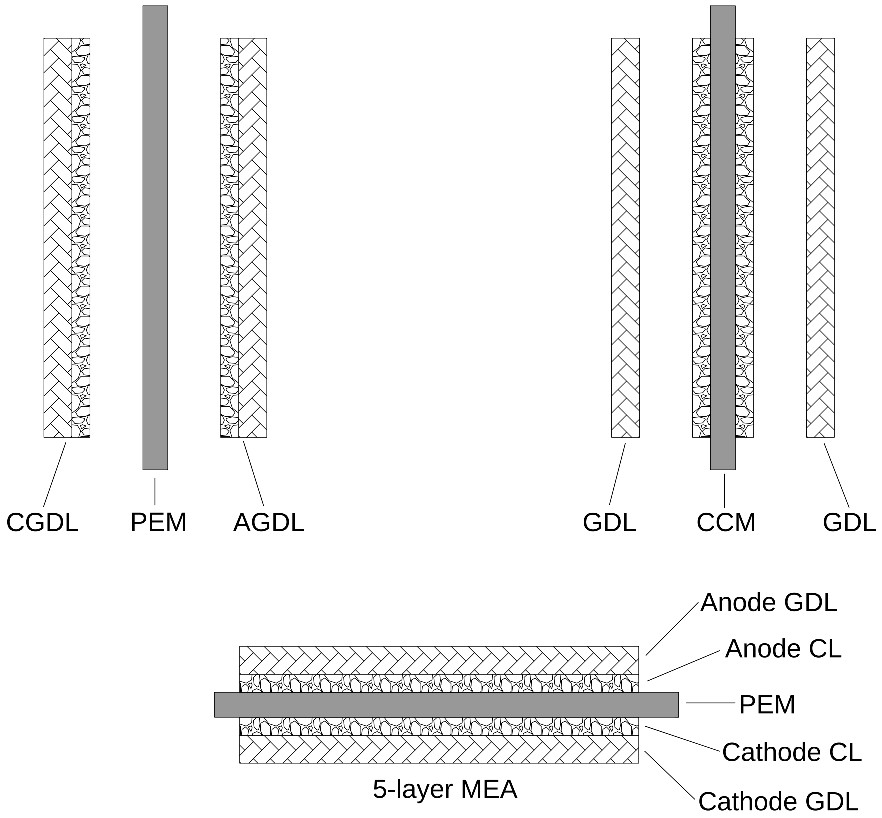

Figure 1.6: Schematic of membrane electrode assembly (MEA) fabrication methods [6]

The characteristics of an ideal CL include those of the GDL (effective transport of gas, water, and electrons) as well as effective ion transport and maximising the number of three phase reaction sites [22, 7, 6]. To accomplish all of these goals, the CL structure is both specific and complex. The CL must be a thin porous active layer containing the maximum number of reactive sites (ie. three-phase interfaces) where gas, electron, ion, and water transport all occur. Figure 1.7 shows an idealized representation of what a single Pt-C particle should look like and illustrating the three phase reaction sites

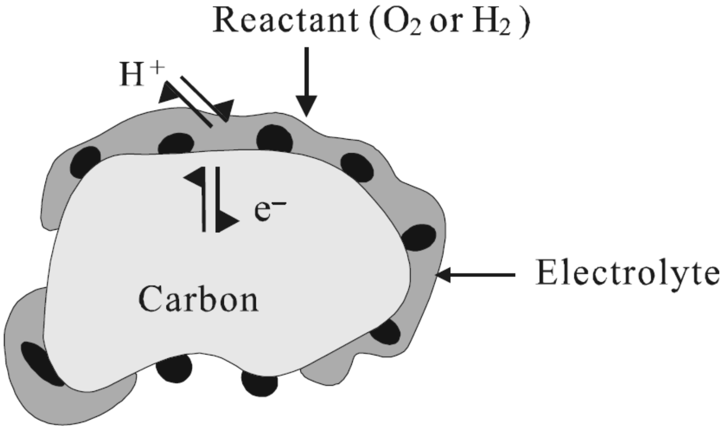

Figure 1.7: Schematic of three phase interface [7]

The CL represents an extremely complex region on the PEM fuel cell which is undergoing extensive research to improve both performance and cost [19]. The gas transport properties are one of many related transport properties that must be optimized [15]. It is important to be able to isolate the effects of manufacturing techniques, material component, and structure have on gas diffusivity through the catalyst layer.

1.3 Thesis Objectives and Scope

The literature review will reveal that experimental work on measuring the diffusion coefficient of gases through fuel cell porous media is relatively limited. Of the methods used to measure diffusion coefficients through porous media, significant work has been performed by researchers at the National Research Council (NRC) located in Vancouver, British Columbia using a modified version of the Loschmidt cell. This work examines the parameters and techniques applied to the modified Loschmidt cell with the following aims.

- Understand the measurement method
- Assess the physical correctness of the method
- Understand the effect of system parameters on accuracy
- Quantify sources of error and uncertainty
- Suggest improvements to the apparatus and method

This thesis makes use of analytical equations, simulations, and experimental work to fully understand the Loschmidt cell analytical technique.

Chapter 2

Background

2.1 Theory of Gas Diffusion

Diffusion refers to the net motion of mass in a single phase without mixing (ie. mechanical or convective mixing). It has been shown by both theory and experiments that diffusion can be a result of pressure gradients (pressure diffusion), temperature gradients (thermal diffusion), external force fields (forced diffusion), and concentration gradients [23, 24]. The focus will be placed on diffusion as a result of concentration gradients (henceforth simply referred to as diffusion). As gas molecules move about randomly without a preferred direction, each species has the tendency to distribute itself evenly throughout the its container[23, 25]. Since both transfer of heat by conduction and transfer of mass by diffusion are a result of random molecular motion, the quantitative expressions are analogous to each other [8, 26, 27]. Fick (1855) first applied the equation of heat conduction derived by Fourier (1822) years earlier to the diffusion of mass [28]. The theory of diffusion states that the rate of mass transfer through a unit area in an isotropic substance is proportional to the concentration gradient normal to the area. The statement expressed as an equation in one-dimensional form is

$$F_x = -D\frac{\partial C}{\partial x} \tag{2.1}$$

where F_x is the rate of transfer per unit area, C is the concentration of the diffusing substance, x is Cartesian direction normal to the section, and D is the proportionality constant known as the diffusion coefficient. The differential equation for diffusion in an isotropic medium can be derived from Equation 2.1 by considering an elemental volume as depicted in Figure 2.1. The lengths of the edges are $2dx$, $2dy$, and $2dz$. The center of the element is point $P(x, y, z)$ and has a concentration of C.

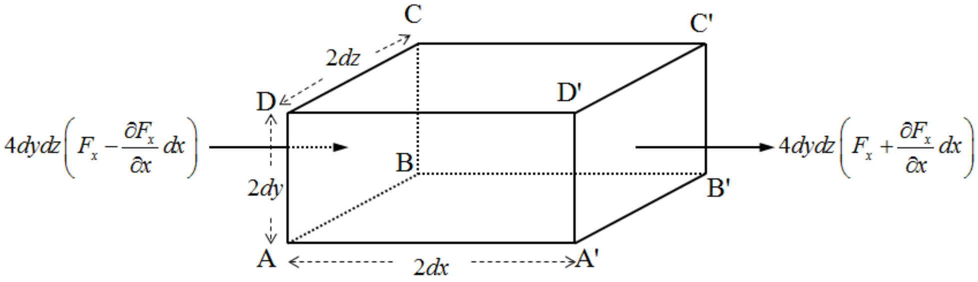

Figure 2.1: Elemental volume for diffusion [8]

Using Taylor's Series and conservation of mass, one can arrive at the following equation

$$\frac{\partial C}{\partial t} + \frac{\partial F_x}{\partial x} + \frac{\partial F_y}{\partial y} + \frac{\partial F_z}{\partial z} = 0 \tag{2.2}$$

Equations 2.2 and 2.1 can be combined to obtain

$$\frac{\partial C}{\partial t} = D(\frac{\partial^2 C}{\partial x^2} + \frac{\partial^2 C}{\partial y^2} + \frac{\partial^2 C}{\partial z^2}) \tag{2.3}$$

or further simplified into vector form to be

$$\frac{\partial C}{\partial t} = \nabla \cdot (D \nabla C) \tag{2.4}$$

Equation 2.4 for one-dimensional diffusion assuming that the diffusion coefficient is constant with respect to concentration can be written as

$$\frac{\partial C}{\partial t} = D \frac{\partial^2 C}{\partial x^2} \tag{2.5}$$

The above discussion is suitable for dilute mixtures where the diffusing substance has a much lower concentration than the medium through which it is diffusing. In the case of a two component gas mixture, the flux of both species must be considered.

$$\begin{cases} F_1 = -D_{12}\nabla C_1 \\ F_2 = -D_{21}\nabla C_2 \end{cases} \tag{2.6}$$

where species are labelled with subscripts 1 or 2 and the diffusion coefficient denotes the diffusion of one species into the other (ie. D_{12} is the diffusion coefficient of species 1 into 2). In the case where there is no net flux ($F_1 + F_2 = 0$) it can be shown that $D_{12} = D_{21}$ and $C_1 + C_2 = C$. Thus, in the case of binary diffusion with no net flux, only one diffusion coefficient is needed. In the case where the net flux is not equal to zero, Equation 2.6 can be defined for a moving coordinate system with velocity $\frac{F_1+F_2}{C}$ or rewritten to define D in a stationary coordinate system. As before, it can be shown that $D_{12} = D_{21}$ [8, 23].

$$\begin{cases} F_1 = -D_{12}\nabla C_1 + x_1 F \\ F_2 = -D_{21}\nabla C_2 + x_2 F \\ F = F_1 + F_2 \end{cases} \tag{2.7}$$

where x is the mole fraction of each component. In the strict sense, binary diffusion with unequal fluxes cannot occur in a system where both the net flux and pressure gradient are simultaneously zero. If the net flux is zero, a small pressure gradient must exist to counter the difference in fluxes. The pressure gradient in diffusing gas mixtures is extremely small and only measurable in specialized capillary experiments [29]. Thus, it is unnecessary to include a pressure gradient term in Equation 2.7 since the pressure effects included in the flux terms. The equations presented are applicable to systems regardless of dependence of the diffusion coefficient on composition, pressure, or temperature.

The Stephan-Maxwell equations describe multicomponent diffusion based on the diffusion coefficients of binary mixtures [29, 30, 28].

$$\nabla x_i = \sum_{j=1}^{\nu} \frac{x_i x_j}{D'_{ij}} \left(\frac{F_j}{C_j} - \frac{F_i}{C_i} \right) \tag{2.8}$$

where i and j denote species, ν is the total number of species in the mixture, and D'_{ij} is the diffusion coefficient which has a dependence on the relationship between species i and j. The slight difference between D_{ij} and D'_{ij} is due to weak composition dependence and thus is reasonable to make the approximation that $D'_{ij} \approx D_{ij}$ [29].

2.2 Correlations for Gas Diffusivity in Porous Media

Diffusion in pores can occur by the three mechanisms of bulk diffusion, Knudsen diffusion, and surface diffusion [31]. For the discussion in this thesis, surface diffusion is not considered. Bulk, ordinary, or Fickian diffusion is discussed in Section 2.1. For Fickian diffusion, the effective diffusion coefficient through a porous material is related to the volume fraction of void space (porosity ϕ) and the length fraction of the tortuous flow path to straight line length (tortuosity τ). The typical case of irregular pore shape and non-constant cross section leads to constrictions offering greater resistance which is not offset by enlargements and so the flux tends to be less than that of a uniform pore shape [32].

Under the assumption of Fickian diffusion, there are a large number equations available to model the effective diffusivity (D_{eff}) through porous networks. The equation below shows a basic relationship for the effective diffusion coefficient through porous media. For unconsolidated porous media, tortuosity ranges between 1.5 and 2.0 [32]. In general, however, tortuosity is not a known value.

$$D_{\text{eff}} = \frac{D\phi}{\tau} \tag{2.9}$$

Other correlations for effective gas diffusion through porous media have been proposed by Bruggeman, Neale and Nader, Tomadakis and Sotirchos, Nam and Kaviany, and Das et al. [33, 34, 35, 36, 37]. Each of these correlations circumvents tortuosity and attempts to estimate diffusion coefficient through porous media as a function of only porosity. Zamel et al. compares the effective diffusion coefficients of several correlations against simulation and experimental results [38, 39] to find that many correlations are not sufficiently accurate when used for fuel cell porous media.

Fick's law fails to fully describe diffusion when gases are very low density, the pores are very small, or a combination of the two. Knudsen diffusion, which accounts for the collision of molecules with the pore walls, becomes an important factor in those cases [28, 32]. The limiting situation for Knudsen diffusion (or flow) is when the mean-free path of the gas molecules is greater than the diameter of the pores and only collision between gas molecules and pore walls occur [31]. When neither mechanism is fully dominant, the effective diffusivity can be found by the combination of Fickian and Knudsen diffusion coefficients as shown in Equation 2.10 [28, 40].

$$\frac{1}{D_{\text{eff}}} = \frac{1}{D_{\text{K,eff}}} + \frac{1}{\mathrm{D}_{12,\text{eff}}} \tag{2.10}$$

where $D_{\text{K,eff}}$ is the effective Knudsen diffusion coefficient and $D_{12,\text{eff}}$ is the effective Fickian diffusion coefficient. The mean-free path of a gas can be found through Equation 2.11 assuming ideal gas and Maxwellian motion in all directions [41].

$$l = \frac{k_B T}{\sqrt{2} P \pi \sigma^2} \tag{2.11}$$

where l is the mean-free path, k_B is the Boltzmann constant, T is the absolute temperature, P is the pressure, and σ is the collision diameter. Using a collision diameters of N_2 and O_2, the mean-free path at standard ambient temperature and pressure is approximately $70nm$ [42]. The pore size of GDL is sufficiently large that Knudsen diffusion is negligible. Diffusion in the much smaller pores of the MPL or CL must account for both Fickian and Knudsen diffusion.

Chapter 3

Literature Review

3.1 Measurement of Effective Gas Diffusion Coefficient of Porous Media

Several methods can be found in literature for measurement of gas diffusion coefficient through porous media. Most of the methods discussed are specifically intended for measurement of fuel cell diffusion media. Some of these measurement techniques are in-situ, making use of the structure and behaviour of the fuel cell to deduce the gas diffusion coefficient through the porous media.

Baker et al. [43, 44] and others [45, 46] used the method of limiting current in a fuel cell to determine mass transport resistances. The limiting current method determines the highest achievable current in the concentration polarization region (where mass flux limitations are dominant) at various inlet O_2 concentrations in an operating fuel cell. Through a simplified one-dimensional model of the fuel cell, the limiting current is related to the effective diffusion coefficient of the entire cell. The overall effective diffusion coefficient can be converted to a total resistance and split into the various contributing resistances to find the resistance through the GDL. The method uses a low flow rate of inlet gas, dry gas, and low O_2 concentration to minimize pressure gradient in the flow channels and water production. The contributing resistance can be split apart through parametric experiments that vary pressures, inlet gas concentration, and material thickness. This method suffers from trying to discern a single material property in a complex system with a variety of uncontrolled variables. The method cannot precisely control or monitor changing concentrations throughout the cell and require estimates and averages to reach an estimate. Further, it is noted by Baker et al. as well as Beuscher that the GDL resistance accounts for approximately 50% or less of the resistance to diffusion observable in this method [44, 45]. The method also requires a large number of polarization curves over a huge range of value for several operating conditions to calculate results. Baker et al. do show that there is good agreement between in-situ limiting current method and ex-situ effective diffusion coefficient measurements [43].

The method of electrochemical diffusimetry, used by Kramer et al. [47] and others [48, 49, 50, 51], infers the effective diffusion coefficient through measurement of electrochemical impedance. Porous media is submerged in an electrolyte solution while a sinusoidal or square waveform of DC current is applied between two electrodes within the electrolyte solution placed on either side of the sample. Comparison of the response of tests with and without the sample lead to an inference of the electrochemical impedance of the sample which is used to calculate a resistance to diffusion and an effective diffusion coefficient through the porous media. Kramer et al. [47] notes that the results obtained using this method are in agreement with the results of Baker et al. [43]. Electrochemical diffusimetry is a relatively quick method of determining the effective diffusion coefficient. A significant weakness of the method is that in materials where Knudsen diffusion (or any non-Fickian diffusion) occurs, the analogy is incapable of accurately accounting for the potential impacts.

LaManna et al. employ a parallel flow mass exchanger to measure the effective diffusion coefficient through fuel cell porous media [52]. The parallel flow mass exchanger technique works by separating two channels with the porous media to be measured. One channel flows humidified gas while the other flows dry gas. Theory allows the calculation of the effective diffusion coefficient from knowing the inlet and outlet humidities of the two channels. LaManna et al. notes that error is minimized by ensuring minimal pressure difference between the two channels and accurate humidity measurements [52]. Despite attempts, the GDL used would be expected to have such high permeability that a nearly imperceptible pressure difference or unequal pressure drop along the two channels will induce some forced convective transport between the channels. Further, the experiment is conducted at 25°C where very little water vapour is held by the air and increases overall measurement uncertainty. In general, results using parallel flow mass exchangers are in agreement with electrochemical diffusimetry results by Flückiger et al. [48].

3.2 The Modified Loschmidt Cell for Measurement of Effective Gas Diffusion Coefficient of Porous Media

The Loschmidt cell or closed tube method for measuring binary gas diffusion coefficients has been modified in several studies for measurement of diffusion coefficient through GDL, CL, and MPL. The modified Loschmidt cell is an ex-situ technique, which means that while current literature covers only gas diffusion measurements through fuel cell porous media, the concept itself can be applied to any form of consolidated porous media.

Modification of the Loschmidt cell to make it capable of measuring the gas diffusivity through a porous medium was first performed by Rohling et al. [53]. The experiment used an in-house constructed Loschmidt diffusion apparatus modified to hold a porous sample near the interface between the two chambers. The porous sample consisted of four GDL layers stacked for a total thickness of 1.40mm. The concentration of CO_2 in a $CO_2 - O_2$ binary mixture was measured using the photothermal deflection (PD) technique described in a previous study [54]. Gas concentration is measured at a point 57.2mm away from the interface of the two chambers and on the same side as the sample. The distance of the gas measurement point from the chamber interface is referred to as the diffusion distance. The study was successful in measuring a binary diffusion coefficient consistent with literature values for the $CO_2 - O_2$ system as well as an effective diffusion coefficient of the porous sample using equivalent diffusive resistances and a resistance network. This study was the first study to use the resistance network method for calculating the effective diffusivity of the sample positioned in a Loschmidt cell. The concept is borrowed from a study by Zhang et al. [55] where diffusive resistances and the analogy of electrical circuit resistance was used to develop a one-dimension model for steady-state gas diffusion through a catalytic monolith. The analogy of electrical resistance for steady-state phenomenon is extensively used in heat transfer and discussed in depth by Incropera et al. and Yovanovich [25, 56]. With the direct analogy between the diffusion of heat and gas [8, 27], the use of resistances and resistance networks for steady-state gas diffusion is shown to be valid. In the case of the modified Loschmidt cell, Rohling et al. offers no specific discussion on the validity of the resistance network method and subsequent studies using the modified Loschmidt cell refer to Rohling et al. the use of the resistance network [57, 39, 58, 59].

Astrath et al. used the modified Loschmidt cell to measure gas diffusion through stainless steel films with differently shaped holes [57]. As series of photoetched MicroEtch Screens samples from Tech-Etch Inc. and a stainless steel sample with laser microdrilled holes from Alase Technologies were tested in the cell. The thickness of the samples ranged from 0.050mm to 0.506mm with well known hole geometry and dimensions. The diffusion distance is 19mm while the full apparatus is 355mm [39]. This experiment uses $O_2 - N_2$ and measures gas using an Ocean Optics FOXY-AL300 oxygen probe. The effective diffusion coefficient of each of the samples was measuring using the modified Loschmidt cell as well as simulated using an FEM package (ANSYS). With pore sizes approximately three orders of magnitude greater than the mean free path of the gases, it was concluded that Knudsen diffusion can be completely ignored. The comparison of the measured and simulated results showed a difference of between 4% and 36%. The differences are attributed the theoretical diffusion being a one-dimensional value and the difference between the cross section of the pores used in calculation compared to the scanning electron microscope (SEM) image of the actual samples. Missing in the discussion is error associated with the resistance network and quantitative determination of the magnitude of each source of error.

Using the same apparatus as Astrath et al., Zamel et al. [39] measured the effective diffusivity of TORAY carbom paper (TPGH-120). The carbon paper is 0.370mm thick and can have a varying degree of Teflon treatment. The study is divided into two groups. The first group of measurements looks at the effect of temperature on the effective diffusion coefficient of an untreated TPGH-120 sample in $O_2 - N_2$. The second group of measurements looks at the effect of various degrees of Teflon treatment on the range of $0\% - 40\%$ in humidified gas ($O_2 - N_2$ with water vapour on both sides). For the first group, the diffusivity of the bulk gas and sample were measured from 25°C to 80°C. The binary diffusion coefficient was found to be consistent with the estimate for bulk gas developed by Fuller et al. [60]. Diffusibility was introduced as the ratio of effective sample diffusivity and bulk gas diffusivity. The value of diffusibility over the temperature range varied between 0.252 and 0.281. It was found that the diffusibility does not change significantly with respect to temperature. For the second group, the diffusibility of the sample was found to fall dramatically with increasing weight percentage of Teflon treatment. With additional porosity measurements, the diffusibility of the sample with respect to porosity was compared to the results of a number of models. It was found that the models significantly over-predict diffusibility. The study mentions only that 60 measurements were performed for each sample and a 95% confidence interval was used for the data. The relatively large difference in diffusibility measurements in group one was not addressed and calculations of experimental error were not performed.

The technique for measuring porous samples was further extended by Shen et al. and used by Chan et al. to measure thin layers of unconsolidated porous fuel cell material on a structural porous substrate backing [58, 59]. Shen et al. used a 60μm thick Al_2O_3 film, referred to as "Anodisc 25", as a substrate to serve as a backing for fuel cell cathode catalyst layers (CCL) $6 - 29\mu$m thick. The substrate material was chosen for its well-defined pore structure, significantly higher effective diffusion coefficient than the CCL, and having small enough pores to prevent penetration of the CCL into the substrate during deposition. The measurements used a diffusion distance of 15.95mm and $O_2 - N_2$. Due to the addition of a secondary layer, three measurements were required to find the diffusivity of the deposited layer, one with no sample, one with only the substrate, and one with a CCL deposited on the substrate. The measured diffusion coefficient of the catalyst layer ranges from $1.12 \times 10^{-7}\text{m}^2/\text{s}$ to $1.84 \times 10^{-7}\text{m}^2/\text{s}$. Shen attributes the large variability in the measurements to the effect of having a very thin CCL and discusses how a small change in the measurements has a huge impact on the diffusivity of the CCL through the use of the resistance network. The pores of the Anodisc 25 and CCL are estimated to be 200nm and $10 - 200$nm, respectively. Since the gases involved have a mean free path in the same order of magnitude, Knudsen effect is expected in the results and is offered as further reasons the weakness of various models for diffusion in porous media. However, Shen erroneously makes the assertion that the appearance of Knudsen diffusion causes the measured diffusivity to be much lower than than the Bruggeman correlation since Zamel et al. demonstrated that the Bruggeman correlation over-predicts even when there is no Knudsen diffusion [39]. As with previous studies, Shen et al. do not justify the use of the resistance network or perform experimental error calculations.

The study by Chan et al. [59] uses the same technique as Shen et al. to measure the effective diffusion coefficient of a micro-porous layer (MPL) deposited onto a GDL substrate as well as the effect of PTFE on the effective diffusion coefficient of GDL [59]. The MPL is a layer sometimes applied to the GDL to improve performance through catalyst layer (CL) localization by preventing intrusion into the GDL and improvement of water management during operation. As with the measurements performed by Shen et al., the MPL has sufficiently small pores such that Knudsen diffusion is a factor. The error for the measurements of effective diffusivity of the sample is calculated to be between 9% and 12% while the error bars shown on figures appear to extend beyond those values.

A study by Unsworth et al. [61] measured the diffusion coefficient of several untreated GDL's from two different manufacturers over a range of temperature. This analysis, unlike previous studies, used the finite length analytical solution to Fick's law (rather than infinite length analytical solution). Also included in the analysis is a discussion of experimental uncertainty which concluded that experimental uncertainty of 2.30% for basic diffusion coefficient measurements. Measurements for the effective diffusion coefficient of the GDL have an uncertainty depending on the ratio of the resistance of the porous sample and the resistance of the rest of the bulk gas from the center of the apparatus to the oxygen probe measurement point.

All of the aforementioned studies record a time-concentration profile at the gas concentration measurement point. The time-concentration data is transformed into a single value for diffusivity (for both situations with bulk gas and with a sample) by matching to an analytical equation derived from Fick's first law and an appropriate set of boundary and initial conditions. Most studies use the solution for Fick's law for an infinite couple presented by Crank [8]. This solution assumes infinite length for both chambers and is used as an approximation for diffusion times sufficiently short such that the gas does not reach the Loschmidt cell boundaries [8, 54]. The limitation is seen in the experimental times for the studies examined being restricted to between 200s and 300s.

Chapter 4

Development of Tools for Analysis

4.1 The Conventional and the Modified Loschmidt Cell

The current study uses an in-house Loschmidt cell as a basis of investigation. The apparatus is bsed on the principles demonstrated by the experimental work of Zamel et al. [39] and is a modified version of the apparatus described by Chan et al. [59]. A diagram of the in-house Loschmidt cell is shown in Figure 4.1.

The conventional Loschmidt cell is a long tube divided into two equal volume (8 and 9) chambers by the sliding gate valve (5). An oxygen gas probe (7) is located in the upper chamber and the distance from the gate valve to the gas probe is also referred to as the diffusion length, x_p. Valves (1-4) are positioned throughout the apparatus to purge and fill the chambers with O_2 and N_2. A modified Loschmidt cell includes a sample holder (6) which holds a thin porous sample between the sliding gate valve and the oxygen gas probe. The in-house Loschmidt cell has a total length of L = 357mm, diffusion length of x_p = 25.9mm, and an inner diameter of d = 20.6mm. To initialize the cell for an experimental run, the sliding gate valve is closed (5b), the upper chamber (8) is filled with dry N_2 gas, and the lower chamber (9) is filled with dry O_2 gas. Oxygen concentration is measured by the oxygen gas probe (7) for the duration of the experiment. The time-concentration data is used the in the data reduction process to find a value for the binary gas diffusion coefficient based on curve fitting to an analytical solutions for Fick's law

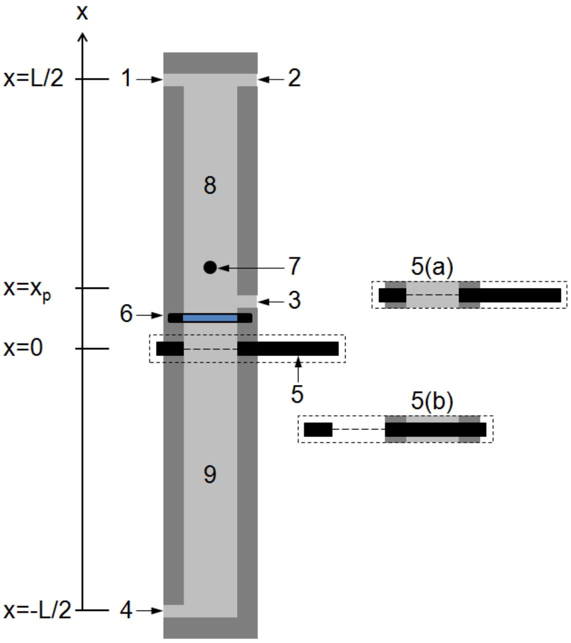

Figure 4.1: Schematic of in-house Loschmidt cell with 1 to 4 - gas inlets and outlets; 5 - sliding gate valve (5a - open gate, 5b - closed gate); 6 - porous sample holder; 7 - location of oxygen probe ; 8 - upper chamber (initially nitrogen); 9 - lower chamber (initially oxygen)

solved for inter-diffusion of a binary gas pair in a long enclosed tube. The data collection procedure for the time-concentration data is the same with or without a porous sample present.

Initialization of the Loschmidt cell creates a stepwise concentration profile that is allowed to change with time once the gate is opened. Figure 4.2a shows an example of the change of O_2 concentration throughout the Loschmidt cell. Figure 4.2b shows a series of time-concentration profiles for various diffusion coefficients that represent typical data sets recorded during a Loschmidt cell measurement. Data shown in Figures 4.2a and 4.2b are found using the analytical solution of Fick's law for a conventional Loschmidt cell. The gradual change of shape for changing binary diffusivity coefficients in Figure 4.2b is what allows the analytical equations to curve fit for the single value of diffusion coefficient.

As discussed in Section 3.2, previous studies used the infinite couple solution to Fick's law which assumes an infinite length for the Loschmidt cell tube. The analytical solution

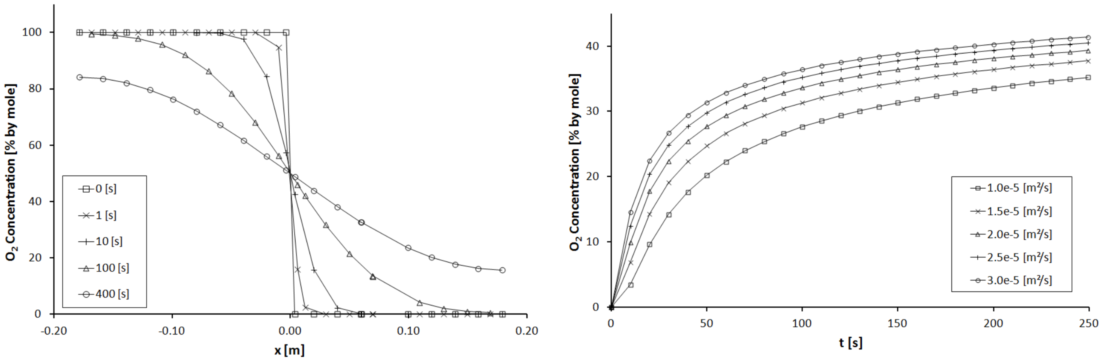

(a) Concentration profile evolution in a Loschmidt cell

(b) Example of typical time-concentration data

Figure 4.2: Visualization of Loschmidt concentration profiles

for the infinite couple as presented by Crank [8] is

$$C\left(x,t\right) = C_{o,t} + \frac{C_{o,b} - C_{o,t}}{2} \operatorname{erfc} \frac{x}{2\sqrt{Dt}} \tag{4.1}$$

with initial conditions

$$\begin{cases} C\left(x>0\right) = C_{o,b} \\ C\left(x<0\right) = C_{o,t} \end{cases} \tag{4.2}$$

where the subscript "o" indicates the initial value, subscripts "t" and "b" indicate "top" and "bottom", respectively, C is the concentration of the measured gas, D is binary gas diffusion coefficient, and x and t are the space and time coordinates. By setting $x = x_p$, Equation 4.1 can be used to approximate the concentration profile with respect to time to mirror the experimental situation. As a condition for the validity of using Equation 4.1, an additional parameter referred to as the "characteristic time" and denoted as τ is introduced

$$\tau = \frac{L^2}{\pi D} \tag{4.3}$$

where D is the binary diffusivity coefficient and L is the total length of the apparatus. It is generally considered that when $t < 0.1\tau$, Equation 4.1 is a valid approximation [8, 54].

The constraint ensures that only a negligible amount of gas has diffused to the ends of the Loschmidt cell and thus has minimal impact on the measured concentration. Substitution of $t = 0.1\tau$ into Equation 4.1 shows that the concentration at the ends of the cell have changed by 3.6% of the initial concentration difference between the two chambers. For a Loschmidt experiment without a sample, the binary diffusion coefficient, D, in Equation 4.1 is adjusted to fit a concentration profile to the experimental data. For modified Loschmidt cell experiments with a porous sample, the data reduction is said to give the equivalent diffusion coefficient, D_{eq}, which represents the combined effect of diffusion through the both the bulk gas as well as the porous sample. D_{eq} is used in the resistance network method to calculate the effective diffusion coefficient through the porous sample, D_{eff}. The resistance network method analyses the space between the sliding gate valve and the oxygen probe by representing the region as diffusive resistances in series.

Figure 4.3a shows the diffusion distance in a conventional Loschmidt cell represented as a single diffusive resistance, R_{bulk}, based on the binary diffusion coefficient of the gas, D_{bulk}. Figure 4.3b shows the diffusion distance in the modified Loschmidt cell represented as either a single equivalent resistance, R_{eq}, based on D_{eq} or as a set of in-series resistance comprised of R_{bulk} and effective resistance of the porous sample, R_{eff}.

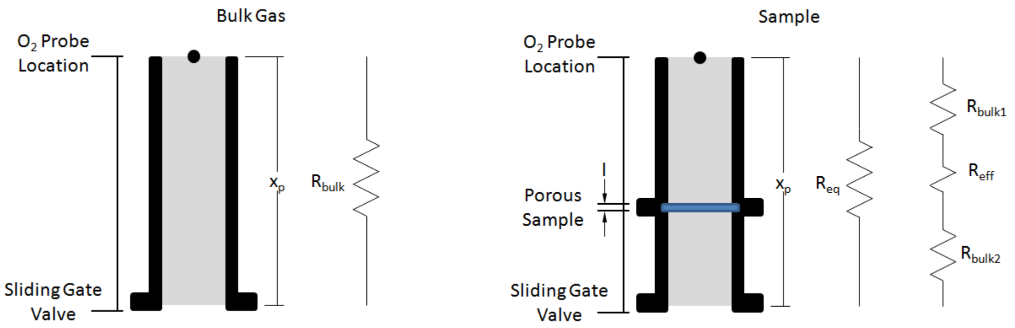

(a) conventional Loschmidt cell

(b) modified Loshcmidt cell

Figure 4.3: Schematic of resistance network

The general expression for a diffusive resistance can be written as

$$R_{=}\frac{\Delta x}{DA} \tag{4.4}$$

where Δx is the distance of diffusion, and A is the cross-sectional area. Heat conduction is very commonly expressed as thermal resistances which is directly analogous to mass diffusion [25, 56] and resistances for gas diffusion is also used by Zhang et al. [55]. The two sets of resistances shown in Figure 4.3b can be written in terms of the distances and diffusion coefficients in an equation. The expressions of the two resistance networks can be equated to give

$$\frac{x_p}{D_{\mathrm{eq}}A} = \frac{l}{D_{\mathrm{eff}}A} + \frac{x_p - l}{D_{\mathrm{bulk}}A} \tag{4.5}$$

which can be simplified to isolate for D_{eff}

$$D_{\mathrm{eff}} = \frac{l}{\frac{x_p}{D_{\mathrm{eq}}} - \frac{x_p - l}{D_{\mathrm{bulk}}}} \tag{4.6}$$

The effective diffusion coefficient through the porous sample found using the resistance network is D_{eff} whereas the true diffusion coefficient through the sample is denoted as D_{sample}. In order to find D_{eff}, two measurements must be performed; one without the porous sample to measure D_{bulk} and one with the porous sample to measure D_{eq}. D_{bulk} is often only measured to verify equipment accuracy while resistance network calculations will use well established literature values for D_{bulk}.

4.2 Changes to Loschmidt Cell

The present study makes use of an in-house modified Loschmidt cell used in previously published experimental work [62]. Before using the apparatus for this study, a significant number of changes were made to the physical apparatus, experimental procedure, and data reduction process. The changes significantly increase the capability, accuracy and operability of the modified Loschmidt cell. A summary of the changes and their impact are provided.

4.2.1 Change to Experimental Procedure

The initialization of the modified Loschmidt cell apparatus requires filling the upper and lower chambers with high purity N_2 and O_2 gas, respectively. In initial stages of experimentation, it was observed that despite the use of nearly pure gas (over 99.99% purity) to purge and fill the chambers, the gas concentration measured by the probe after six minutes would often be less than 99% purity. This was likely due to the two mass flow controllers having a relatively low flow rate of 100mL/min being unable to effectively purge the two chambers. The previous experimental procedure was also unable to measure the concentration of the lower chamber following the purge and fill procedure. The assumption of a concentration for the lower chamber initial concentration introduces a significant amount of uncertainty in the value of D. Changes were made to the experimental procedure to alleviate the requirement of extremely long purge times as well as the need to assume an initial concentration for the lower chamber.

A partial purge to an intermediate concentration, even if it is significantly below 100% purity, is allowable since it is the initial concentration difference between the two chambers that is critical rather than the concentration of each individual chamber. The experimental procedure was modified with the primary goal of using the single oxygen gas probe to measure the initial concentration of both the upper and lower chambers during system initialization. The experimental procedure is provided below with Figure 4.4 detailed for visualization.

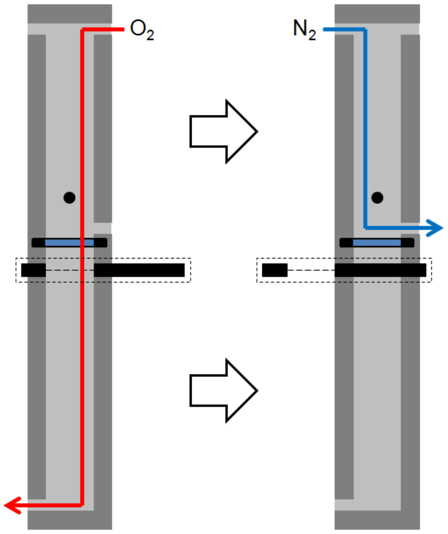

Figure 4.4: Schematicc of purge and fill procedure

1. The gate valve is opened and O_2 is flowed from the top to the bottom of the Loschmidt

cell to purge the both chambers

2. O_2 flow is stopped, all valves are closed, and O_2 concentration measurement is recorded as the initial concentration of the lower chamber
3. Sliding gate valve is closed to seal the bottom chamber
4. N_2 is flowed from the top to the bottom of the upper chamber
5. N_2 flow is stopped, all valves are closed, and O_2 concentration measurement is recorded as the initial concentration of the upper chamber
6. Continuous recording of O_2 concentrations begin for the time-concentration data
7. The sliding gate valve is opened to begin the experiment
8. After sufficient time has elapsed in the experiment, concentration measurements are halted and the apparatus is ready to undergo reinitialization

Measuring of both initial concentrations has the added benefit of allowing a much shorter purge time. As the miscellaneous gas concentration drops below 2%, it takes significantly longer to increase the purity of the purge. By allowing for a partial purge, the purge time can be significantly shortened and the number of measurements that can be recorded per hour is greatly increased. Using typical settings, a single experimental measurement takes approximately 20 minutes.

4.2.2 Use of Finite Length Analytical Solution

As outlined in Section 3.2, previous studies used the infinite length solution to Fick's law (Equation 4.1) as the fitting equation. In order to use the infinite length solution, the overall time of the experiment is limited so that only a negligible amount of gas reaches the boundary and has minimal impact on the concentration profile at the oxygen probe location. With the addition of impermeable boundaries at the ends of the Loschmidt cell, the boundary conditions can be written as

$$\left(\frac{\partial C}{\partial x}\right)_{x=\pm\frac{L}{2}} = 0 \tag{4.7}$$

$$C\left(-\frac{L}{2} < x < 0\right) = C_{o,b} \tag{4.8}$$

$$C\left(0 < x < \frac{L}{2}\right) = C_{0,t} \tag{4.9}$$

The finite length solution can be shown to be

$$C\left(x,t\right) = \frac{C_{o,b} + C_{o,t}}{2} - \left(C_{o,b} - C_{o,t}\right)\frac{2}{\pi}\sum_{m=0}^{\infty}\left\{\frac{e^{-\frac{(2m+1)^2\pi^2 Dt}{L^2}}}{2m+1}\sin\left[\frac{\left(2m+1\right)\pi x}{L}\right]\right\} \tag{4.10}$$

where the subscript o indicates initial value, subscripts t and b indicate “top” and “bottom” respectively, C is the gas concentration, and L is the total length of the cell. The terms of the infinite series can be seen to reduce in value with increasing time, t, and element number, m. In actual use, the value of Equation 4.10 can only be approximated by calculating a sufficiently large number of elements such that the sum of the discarded terms of the infinite series are negligible. The value of each successive element reduces linearly with the value of m while reducing exponentially with t. This means that a concentration at a small time will require significantly more elements to approximate than a concentration at a large time. In general, this study uses 1000 elements to approximate the concentration. This large number of elements is shown to give sufficiently accurate concentrations for times as small as $0.1s$. Equation 4.10 is significantly more cumbersome to implement than Equation 4.1 due to the infinite series. However, this study chooses to use the finite length solution in order to avoid the limitations on the length of the experiment. While several studies note the existence of a finite length solution, a full derivation was not found. A derivation is provided in Appendix A.

4.2.3 Addition of Temperature Control

The two chambers of the Loschmidt cell were machined from rectangular blocks of solid aluminium which has extremely high thermal conductivity. Thus, to add temperature control to the apparatus, a series of holes were drilled in the remaining bulk material of the two chambers and connected to a Thermo Scientific FTE-7 temperature bath using a parallel flow manifold configuration. The temperature bath is capable of maintaining temperatures between −15°C and 80°C depending on the working fluid used. Along with the high conductivity of the primarily aluminium construction and parallel flow configuration, the entire apparatus is externally insulated to help promote the highest degree of temperature uniformity. Figure 4.5 shows a schematic of the assembly.

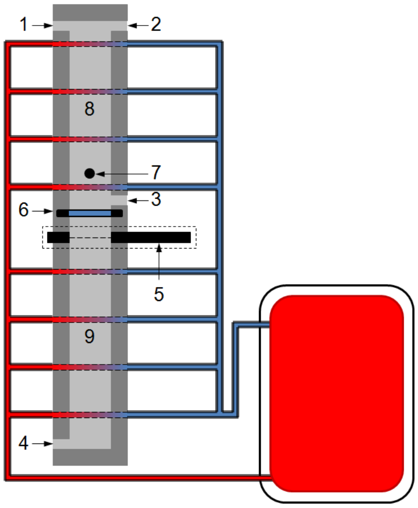

Figure 4.5: Schematic of thermal bath and manifold configuration

Three thermocouples are mounted on the system. Two thermocouples monitor the chamber temperatures at the center of the upper and lower chambers while the third is mounted externally to measure ambient temperature. During experimentation and calibration procedures, the thermal bath is capable of achieving temperatures in the two chambers within 0.05°C of each other.

4.2.4 Oxygen Sensor Accuracy

The oxygen probe in the Loschmidt cell uses a technique known as phase fluorometry to measure oxygen concentration. The sensor tip is coated with ruthenium which fluroesces when excited by a 470nm LED source [63]. The fluorescence is quenched during collisions with oxygen molecules which are diffused into the proprietary ruthenium complex containing sol-gel tip coating. Oxygen, rather than other molecules in the air, is able to quench the fluorescence because of its triplet molecule [64]. The remaining light is passed back through the optical fibre to the spectrometer to measure a phase shift, τ. Calibration involves correlating a series of τ values with corresponding an oxygen concentrations.

This measurement technique effectively measures the partial pressure of oxygen in the air surrounding the probe tip. As such, the measurements are influenced by both temperature and pressure. The temperature is already precisely controlled through the thermal bath. The apparatus operates at atmospheric pressure and changes in local weather patterns have been observed to be detrimental to the accuracy of the oxygen concentration measurements. Furthermore, the manufacturer notes that the oxygen sensor experiences a sensor drift of 0.01% of full scale for each hour of continuous operation. All of the challenges were overcome by performing once or twice daily oxygen probe calibrations. This ensures that the pressure of the calibration and subsequent experiment are negligibly different. The frequent calibration also renders the sensor drift undetectable.

4.2.5 Automation of Test and Calibration Procedure

In coordination with the changes to the test procedure in Section 4.2.1, the oxygen probe calibration procedure was also changed. Calibration of the oxygen probe is done by setting the mass flow controllers (MFC's) for the N_2 and O_2 such that a known concentration of O_2 is passing the oxygen gas probe and the τ reading can be recorded. This is repeated for a series of points from 0% to 100% O_2 so that a polynomial fit can be generated for the concentration-τ relationship to use as a calibration. As noted in Section 4.2.4, calibrations are specific to a single temperature and pressure. The previous procedure required the operator to shut down the apparatus, make valve plumbing changes, and manually set each O_2 calibration concentration and record the corresponding τ. In the new arrangement, both gasses are connected to the top of the upper chamber. The calibration follows the steps outlined below:

1. The sliding gate valve is closed so seal the upper chamber
2. Both inlet valves at the top of the upper chamber as well as a valve at the bottom are opened
3. Mass flow controllers are set to flow a known oxygen percentage from the top to the bottom of the upper chamber

4. Once the τ value on the oxygen probe reaches steady-state, the τ value is recorded along with the corresponding oxygen concentration
5. Mass flow controllers are set to flow a new oxygen concentration and step 4 is repeated until all pre-set oxygen concentration values have a corresponding τ
6. Sliding gate valve is opened and all gas valves are closed

Figure 4.6 shows a schematic of the apparatus during calibration.

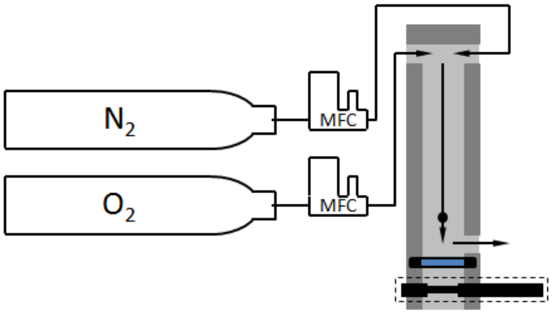

Figure 4.6: Schematic of oxygen probe calibration arrangement using mass flow controllers (MFC's)

The change of gas inlet and outlet arrangement allows the apparatus to switch between calibration and experimentation modes without manual intervention. Both the calibration and experimentation procedure (discussed in Section 4.2.1) are fully automated in LabVIEW. The LabVIEW procedure allows the operator to set calibration and a batch of experiments to be run sequentially. A typical calibration requires approximately 2 hours while a single experimental measurement requires 20 minutes. The automation and streamlining of the apparatus procedures means that minimal operator involvement is required. The automated calibration also makes daily calibrations viable and helps to resolve many issues such as ambient pressure changes and oxygen sensor drift.

4.2.6 Probe Distance Adjustment

The distance between the center of the apparatus (center of the gate valve) and the oxygen probe is a critical fitting parameter that has a large impact on the value of the diffusion coefficient found through curve fitting. Over the course of making modifications to the apparatus, the gaskets fitting around the sample were changed and ultimately resulted in a thicker gasket layer. This led to a small gap remaining between the upper and lower chambers when the two chambers are clamped together to form a seal. Figure 4.7 illustrates how the gaskets lead to the gap.

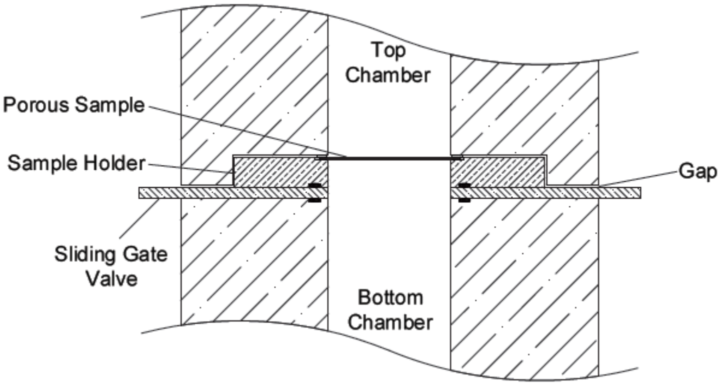

Figure 4.7: Schematic of gap between top and bottom chambers as a result of loading a sample

During testing, it was found that tests with and without a porous sample require different gasket configurations. This constantly changing gasket configuration causes a slight variation the gap width varies depending on the exact clamping pressure applied as well as the specific porous sample mounted in the cell. The change, while very small, is significant enough to introduce error into the measurements. To eliminate error stemming from an inaccurate probe distance, the gap is measured for each new porous sample loaded into the apparatus and the probe distance is adjusted during the curve fitting process.

4.3 Development of Curve Fitting Algorithm

As a result of the full automation of the experimental procedure, the output format of the experimental data is also standardized. Table 4.1 lists the values that are recorded for each experimental run.

The curve fitting uses the two initial concentrations, $C_{o,t}$ and $C_{o,b}$, and the two corresponding arrays of time and concentration data. The experimental data is fitted to the

Table 4.1: Summary of standard output parameters for automated Loschmidt cell tests

Batch Name	-
Time Stamp	YY/MM/DD/hh/mm
Initial Conc. - Top [%O_2 by mole]	$C_{o,t}$
Initial Conc. - Bottom [%O_2 by mole]	$C_{o,b}$
Measurement Time Interval [s]	$t_1, t_2, t_3, \ldots, t_n$
Oxygen Conc. [%O_2 by mole]	$C_1, C_2, C_3, \ldots, C_n$
Temperature - Top [°C]	$T_{1,t}, T_{2,t}, T_{3,t}, \ldots, T_{n,t}$
Temperature - Bottom [°C]	$T_{1,b}, T_{2,b}, T_{3,b}, \ldots, T_{n,b}$

finite length analytical solution to Fick's law in Equation 4.10 (derived in Appendix A). Using an initial guess for the diffusion coefficient, an analytically calculated concentration is found for each point in time of the experimental data. A error is found between corresponding values of analytical and experimental concentration at each time and are used to find the root-mean-square (RMS) of the errors for all time intervals. The RMS error is used in a Newton-Raphson iteration scheme to solve for the value of the diffusion coefficient which results in the closest fit. The expression used for RMS error is given as

$$\mathrm{RMS}\left(D\right) = \left\{ \frac{1}{m} \sum_{n=1}^{m} \left[C\left(x_p, t_n, D\right) - C_n \right]^2 \right\}^{\frac{1}{2}} \tag{4.11}$$

where m is the total number of experimental points, x_p is the oxygen probe location, t_n is the time of the nth measurement, C_n is the nth concentration measurement, and D is diffusion coefficient. The minimum value for RMS must be found to reach the value of D that best fits the experimental data. Thus, the Newton-Raphson method is used to find the root to the first derivative of RMS error (looking for a minima). Since the equation for RMS error is not differentiable, finite-difference approximations are used to approximate the first derivative of RMS error

$$\mathrm{RMS}'\left(D\right) \approx \frac{\mathrm{RMS}\left(D + rD\right) - \mathrm{RMS}\left(D - rD\right)}{2rD} \tag{4.12}$$

as well as the second derivative of RMS error

$$\mathrm{RMS}''(D) \approx \frac{\mathrm{RMS}(D+rD) - 2\mathrm{RMS}(D) + \mathrm{RMS}(D-rD)}{(rD)^2} \tag{4.13}$$

where r is the "perturbance ratio" which is used in favour of a standard finite difference value. This is done since the magnitude of D is unknown and having the preturbance scale with D helps promote stability during iteration. Thus, an estimate of the derivative of RMS error at D requires calculations of RMS error at $D - rD$, D, and $D + rD$. A single step of the Newton-Raphson iteration is

$$D_{i+1} = D_i - (1-\omega)\left[\frac{\mathrm{RMS}'(D_i)}{\mathrm{RMS}''(D_i)}\right] \tag{4.14}$$

and the full approximation expression is

$$D_{i+1} \approx D_i - (1-\omega)\left\{\frac{rD_i\left[\mathrm{RMS}(D_i+rD_i) - \mathrm{RMS}(D_i-rD_i)\right]}{2\left[\mathrm{RMS}(D_i+rD_i) - 2\mathrm{RMS}(D_i) + \mathrm{RMS}(D_i-rD_i)\right]}\right\} \tag{4.15}$$

where ω is the relaxation factor used to enhance stability. Equation 4.15 shows that each Newton-Raphson scheme has the potential to be somewhat computationally expensive when calculating a large set of experimental data and the finite length solution (Equation A.16) is using a large number of elements to approximate the infinite series. Convergence is determined by checking that the value of $|D_{i+1} - D_i|$ is less than 0.1% of D_{i+1}.

Before applying the curve fit algorithm, two key parameters must be determined with significant accuracy. Since the data logging begins before diffusion is allowed to occur, a time offset must be applied to shift data so that diffusion begins at $t = 0$. The value is especially critical since RMS error is calculated only on the vertical axis and a slight offset in time (horizontal axis) can greatly skew the converged value for the diffusion coefficient. Close examination of the concentration measurements early in the experiment where there is a steep rise in the concentration of oxygen can give a very accuracy estimate of the offset time. Figure 4.8 shows twenty sets of experimental data with an analytical fitting curve for the first few seconds of diffusion.

The offset was found to be $36.75s$. Due to the automation of the data logging and gate valve opening, the apparatus operates extremely consistently and thus this offset

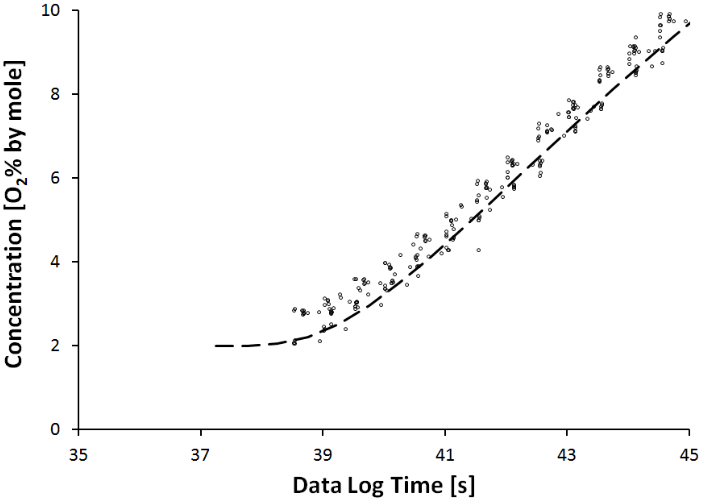

Figure 4.8: Determination of the data log offset time from 20 overlapped experiments

time is used as the standard constant for all experimental curve fitting. The second key parameter is the distance of the oxygen probe from the center line of the gate valve. The exact distance is difficult to measure since the probe is a long flexible fibre optic cable in a thin walled sheath and any attempt at physical measurement causes the probe to deflect. The exact distance was found by measuring the diffusion coefficient of the $O_2 - N_2$ binary pair and tuning the probe distance to match well established literature values. The standard distance with no gap between the two chamber bodies was found to be 25.9mm. Any measured gap during subsequent testing was added to this value.

4.4 Development of One-Dimensional Loschmidt Simulation

For a modified Loschmidt cell with a porous sample, there is no analytically derived equation that is capable of fully encompassing the conditions. Specifically, inclusion of a sample means that the diffusion coefficient is no longer constant throughout the cell. To accurately calculate the concentration change with time for a modified Loschmidt cell, a one-dimensional simulation was developed in MATLAB with the same geometry as the physical apparatus available in-house [59]. Making use of the direct analogy between heat and mass transfer, a large section of the code was borrowed from source code developed for heat transfer. The simulation is built on a the generic equation for conservation of a scalar quantity and allows for diffusive transport between control volumes. The simulation solves the conservation of mass equation using a multigrid solution algorithm. Neumann boundary conditions were applied at the edge of the calculation domain such that the concentration gradient is zero and diffusion of mass is zero. Initial concentrations are set for the top and bottom chamber based on user inputs. Details regarding the construction and validation of the heat transfer oriented source code can be found in the documentation for ME663: Computational Fluid Mechanics [65].

Key features implemented for the simulator include target time stepping for directed output, adaptive meshing, and control volume mapping. The target time stepping involves the simulator accepting an array of times which will in turn modulate the time step size to ensure steps fall exactly at the given times to remove the need for interpolation. This feature allows the simulator produce data sets to be directly compared to experimental data and removes error through interpolation. Adaptive meshing is used to correctly size control volumes with the changing thickness of the porous samples, ensure that the oxygen probe coincides with the node of a control volume, and ensure that the edges of the sample are represented as control volume edges. All of the above is done to reduce the instances where estimations related to simulation have an impact on the accuracy of the results. Control volume mapping was implemented to reduce the total number of control volumes strategically in certain regions without negatively impacting the accuracy. The base parameters for the simulation are based on the physical Loschmidt cell available in house. Table 4.2 give a summary of the simulation parameters.

The meshing of the calculation domain requires input of five geometric dimensions for the Loschmidt cell. Figure 4.9 shows a schematic of the dimensions required for the simulation.

The point x_1 is arbitrarily set as zero and indicates the center of both the sliding gate valve and the entire apparatus. A control volume edge is placed at x_1 so that the initial stepwise concentration can be accurately applied. Between x_2 and x_3 is the sample. In the sample region, the control volume size is highly variable to minimize the smearing effect of control volumes as well as ensure that control volume edges coincide with sample edges. x_4 indicates a probe location and is used to ensure that a control volume node coincides with

Table 4.2: Loschmidt cell and simulation parameters

Gas Pair	O_2 - N_2	
Measured Gas	O_2	
Probe Location	25.9mm	x_p
Apparatus Length	357.0mm	$\approx 15x_p$
Sample Location	6.35mm	$\approx 0.25x_p$
Sample Thickness	$5 - 10000\mu$m	$0.0002x_p - 0.4x_p$
Control Volume Size	0.25mm	$\approx 0.01x_p$
Sample Control Volumes Size	0.125mm	$\approx 0.005x_p$
Time Step Size	0.025s	

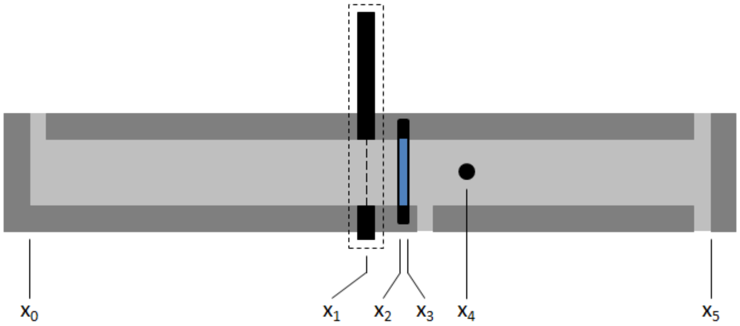

Figure 4.9: Dimensions required to mesh the computational domain

that point to reduce distortion of the concentration value. The two regions from x_0 to x_1 and x_4 to x_5 are where the mapping functions are applied. As the control volumes approach the edges of the apparatus (x_0 and x_5), the length of the control volumes increases. The mapping function reduces the number of control volumes by a factor of three without significant impact on accuracy.

The presence of a sample in the Loschmidt cell causes there to be a sudden change in diffusion coefficient between bulk gas and sample control volumes. The source code uses the properties of both control volumes to calculate the transport between the control volume nodes. Figure 4.10 shows a schematic of the general one-dimensional scheme for transport between two control volumes with unequal size and generalized conductivity.

The transport is calculated between the nodes of each control volume along the line

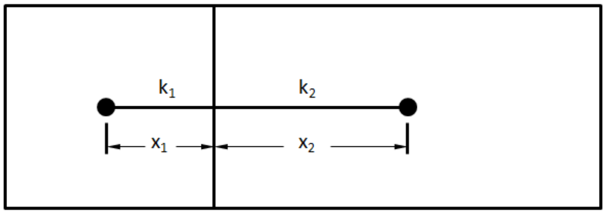

Figure 4.10: Illustration of transport of properties between two control volumes

connecting them. The source code averages the two conductivities $(0.5k_1 + 0.5k_2)$. This method is acceptable when the change in the control volume size or transport properties is gradual and the mesh is sufficiently refined to make errors negligible. In the case of the Loschmidt cell with a sample, the step change in diffusion coefficient generates errors that cannot be efficiently overcome through mesh refinement. A good illustrative example is when one of the control volumes has a conductivity of zero, the simple averaging scheme will still allow for flow between the two nodes. To correct this issue, a resistance based averaging scheme was used where

$$k = \frac{1}{\frac{x_1}{k_1} + \frac{x_2}{k_2}} \tag{4.16}$$

The time step and control volume size shown in Table 4.2 have been tested for convergence. For all cases, mesh parameters are run using a bulk gas diffusivity of $2.00 \times 10^{-5}\mathrm{m}^2/\mathrm{s}$, sample diffusivity of $4.00 \times 10^{-6}\mathrm{m}^2/\mathrm{s}$, sample thickness of $1000\mu\mathrm{m}$, and the geometry given in Table 4.2. Each case is simulated and the time-concentration data at the probe position is recorded as an output (imitating a physical experiment output). The output for each case is put through the curve fitting algorithm to produce a single diffusion coefficient. The change in the diffusion coefficient is used to evaluate whether a specific parameter has led to a grid independent solution.

Unless otherwise indicated, the simulation uses the parameters outlined in Table 4.2. Tables 4.3-4.6 give a summary of the grid independence studies for time step size, control volume size, sample control volume size, and use of mapping function.

The simulation can also be validated against the analytical equations by simulating simple binary gas diffusion using a range of diffusivity values and using the curve fitting algorithm to match for a diffusivity. Table 4.7 shows that the matched diffusivity is the ex-

Table 4.3: Time step size independence study

Time Step Size [s]	$D_{\mathrm{eq}}[\mathrm{m}^2/\mathrm{s}]$
0.2	9.337×10^{-6}
0.1	9.346×10^{-6}
0.05	9.351×10^{-6}
0.025	9.354×10^{-6}
0.0125	9.355×10^{-6}

Table 4.4: Control volume size independence study

Control Volume Size [mm]	$D_{\mathrm{eq}}[\mathrm{m}^2/\mathrm{s}]$
2	9.348×10^{-6}
1	9.353×10^{-6}
0.5	9.354×10^{-6}
0.25	9.354×10^{-6}
0.125	9.354×10^{-6}

Table 4.5: Sample control volume size independence study

Control Volume Size [mm]	$D_{\mathrm{eq}}[\mathrm{m}^2/\mathrm{s}]$
0.25	9.354×10^{-6}
0.125	9.354×10^{-6}
0.0625	9.354×10^{-6}

Table 4.6: Mapping function independence study

Without Mapping	9.354×10^{-5}
With Mapping	9.355×10^{-5}

act same as input diffusivity and demonstrates that the simulation is capable of accurately calculating diffusion in the Loschmidt cell.

The time step size and mapping of the control volumes is seen still have some impact on results but it is judged to be sufficiently small to be acceptable. This compromise is

Table 4.7: Validation of the simulation against analytical solution

Input Diffusivity [m^2/s]	Matched Diffusivity [m^2/s]	Error [%]
5.000×10^{-6}	4.998×10^{-6}	-0.03
1.0000×10^{-5}	1.0000×10^{-5}	0.00
1.5000×10^{-6}	1.5001×10^{-5}	0.00
2.0000×10^{-6}	1.9997×10^{-5}	-0.01
2.5000×10^{-6}	2.4990×10^{-5}	-0.04
3.0000×10^{-6}	2.9983×10^{-5}	-0.06
3.5000×10^{-6}	3.4976×10^{-5}	-0.07
4.0000×10^{-6}	3.9971×10^{-5}	-0.07

made to dramatically increase the speed of the simulations.

4.4.1 Determination of Error in the Resistance Network Method

The error of the resistance network is determined by substituting the one-dimensional simulation for the experimental apparatus in the data generation step. The simulation can be supplied with a set of input parameters to produce sets of data mimicking experimental data. The simulation outputs are then put through the same data reduction process as experimental data to find a calculated value of D_{eff}. The calculated D_{eff} can be compared with the input D_{sample} to find the error introduced by the resistance network. Figure 4.11 is a flow chart representing the method that is used to find the error caused by the resistance network.

Using the process depicted in Figure 4.11 for a range of simulation input parameters will reveal magnitude and behaviour of the error introduced by using the resistance network method.

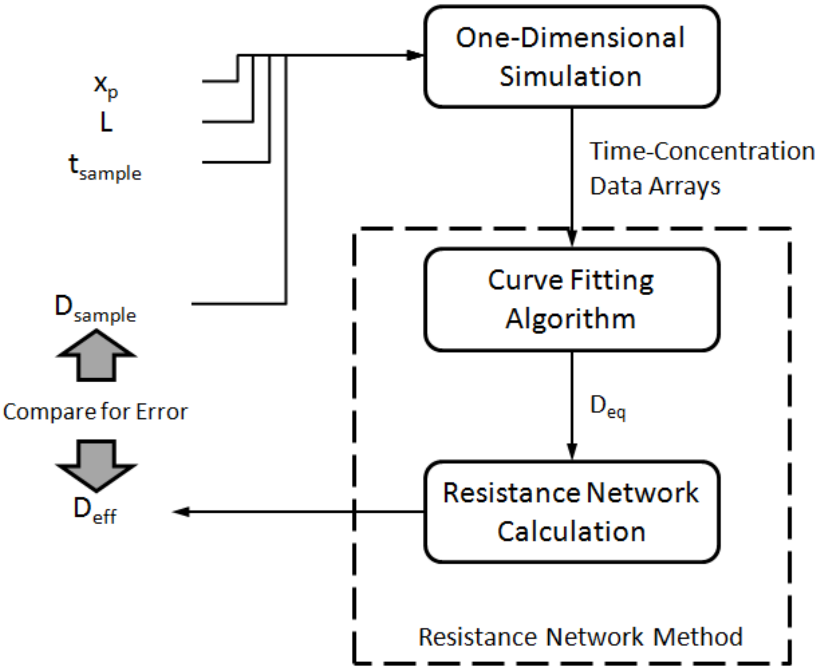

Figure 4.11: Method used to determining the error resulting from the resistance network method

Chapter 5

Results and Discussion

5.1 Resistance Network Discussion

The resistance network used for calculating sample diffusivity for the modified Loschmidt cell is analogous to the resistance based analysis used in heat transfer. the derivation of the resistance network in heat transfer makes the assumption of steady-state [25, 56]. The change in concentration observed in the Loschmidt cell is is governed by one-dimensional Fick's law

$$J_x = -D\frac{dC}{dx} \tag{5.1}$$

where J_x is the flux per unit area in the x-direction, D is the gas diffusion coefficient, and C is the concentration of the diffusing species. As the concentration in the cell changes from the initial stepwise profile (shown in Figure 4.2a), it is clear that flux in the Loschmidt cell is variable with respect to time and location. Furthermore, fitting some D_{eq} to the analytical equation for a Loschmidt test with a porous sample is not strictly valid since it assumes that the entire calculated region has a diffusivity equal to D_{eq} rather than D_{bulk} for most of the cell and D_{sample} for the porous sample. The finite length analytical solution to Fick's law is also elliptical in nature. This means that while the resistance network is only concerned with the diffusion distance between the center of the cell and the gas probe, changes to the concentration in any region of the cell can impact the concentration (to varying degrees) the rest of the cell. Figure 5.1 gives an example of how an sample placed outside of the resistance network calculation domain can still impact concentration. The sample is 1.5mm and has a diffusion coefficient only 1/50th that of the binary gas. The calculation was performed using the one-dimensional simulation.

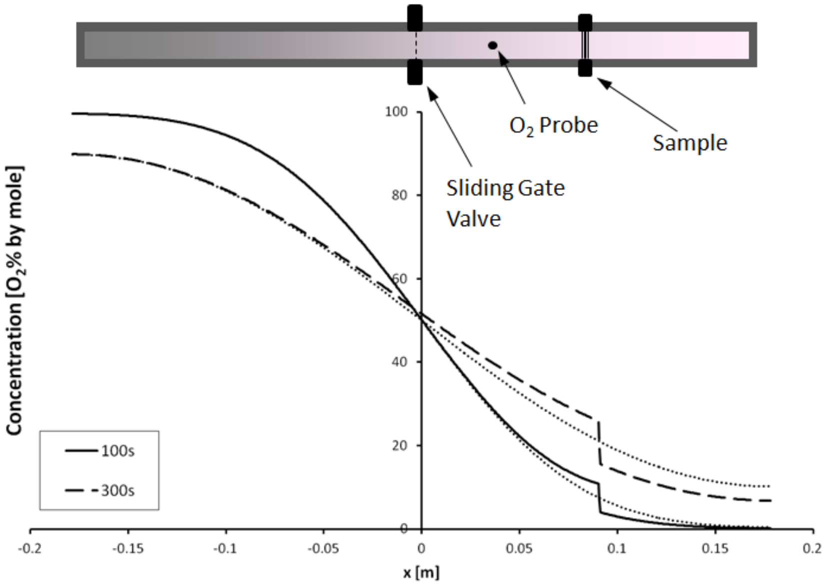

Figure 5.1: Demonstration of elliptical behavior where a sample outside of resistance network location still has an impact

Figure 5.1 shows the concentration profile throughout the apparatus after 100s and 300s both showing the impact of the porous sample and the assumed profile when using an equivalent diffusion coefficient. The figure shows that the porous sample causes the actual concentration profile to deviate from the assumed equivalent profile throughout the entire cell. There is also a concentration change through the sample is approximately proportional to its thickness and the concentration gradient proportional to the sample diffusion coefficient. The figure helps to demonstrate how the resistance network method does not completely fit the situation and has the potential to introduce errors into the value of the diffusion coefficient.

A more appropriate application of the resistance network would be measuring of the diffusion coefficient through a porous sample within a two bulb apparatus . Figure 5.2

shows a schematic of the two bulb apparatus with a porous sample inserted in the tube connecting the two bulbs. With sufficiently large volume on either side, the concentration profile between the two bulbs can reach steady-state. The two bulb method is is considered as accurate as the Loschmidt cell but is significantly slower to implement since quasi-steady state must be reached [29]

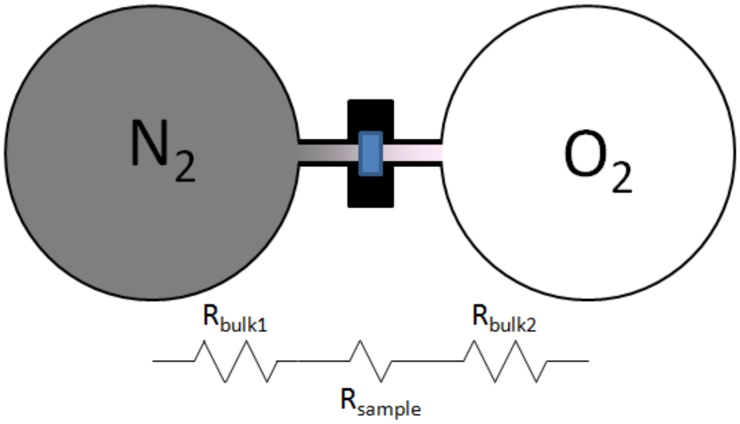

Figure 5.2: The two bulb method with a porous sample where the bulbs are sufficiently large to allow for a steady-state concentration gradient through the connecting tube

The discussion shows that the assumptions of the resistance network does not conform with the modified Loschmidt cell. It is likely that application of the method will introduce errors into the measurement for the porous sample effective diffusion coefficient.

5.2 Dimensionless Analysis

Fick's law in Equation 2.5 can be expressed in generalized dimensionless forms by introducing dimensionless concentration, θ, distance, x^*, and time, Fo, as follows:

$$\theta = \frac{C - C_{o,t}}{C_{o,b} - C_{o,t}} \tag{5.2}$$

$$x^* = \frac{x}{x_p} \tag{5.3}$$

$$\mathrm{Fo} = \frac{Dt}{x_p^2} \tag{5.4}$$

where x_p is the distance between the gate valve and the oxygen probe (also called the diffusion distance) and is used as the "characteristic length". x_p was selected rather than the total length of the apparatus, L, since the concentration profile shape is based on the location of the gas probe. Substitution of the dimensionless parameters into Fick's law results in

$$\frac{\partial\theta}{\partial\mathrm{Fo}} = \frac{\partial^2\theta}{\partial\left(x^*\right)^2} \tag{5.5}$$

and the finite length solution to Fick's law is also expressible in dimensionless terms as shown

$$\theta\left(x^*, \mathrm{Fo}\right) = \frac{1}{2} - \frac{2}{\pi}\sum_{m=0}^{\infty}\left\{\frac{e^{-\frac{(2m+1)^2\pi^2 Fo}{(L^*)^2}}}{2m+1}\sin\left[\frac{(2m+1)\,\pi x^*}{L^*}\right]\right\} \tag{5.6}$$

where L^* is dimensionless total apparatus length equal to L/x_p. Application of the dimensionless parameters causes previously different concentration-time profiles to collapse into a single characteristic curve.

Dimensionless parameters are very useful in this analysis. In Equation 5.6, when looking at the concentration of gas at the oxygen probe location, x^* is constant and the only variable controlling θ is Fo. In terms of a parametric study, rather than investigating the effects of changing $C_{o,b}$, $C_{o,t}$, t, D, and x_p only the effect of Fo needs to be investigated. The form of the dimensionless parameters also show more clearly how each individual variable impacts the time-concentration data. For dimensionless concentration, θ, the form shows that the driving force in the diffusion is not absolute concentration difference but rather the fraction of the maximum concentration difference that initially exists $(C_{o,b} - C_{o,t})$. Dimensionless distance, x^*, reveals that instead of absolute length, it is relative length that controls the behaviour. Dimensionless time, Fo, reveals that time, space, and transmissivity (diffusivity) are interrelated. Plotting data from Loschmidt cell test (without a porous sample) of varying diffusion coefficients on dimensionless axes causes all concentration profiles to collapse into a single characteristic curve. The characteristic curve is demonstrated by Figure 5.3 which shows experimental data for Loschmidt cell tests for temperatures of 25°C, 50°C, and 70°C which correspond to diffusion coefficients of $2.0 \times 10^{-5}\mathrm{m}^2/\mathrm{s}$, $2.3 \times 10^{-5}\mathrm{m}^2/\mathrm{s}$, and $2.6 \times 10^{-5}\mathrm{m}^2/\mathrm{s}$, respectively.

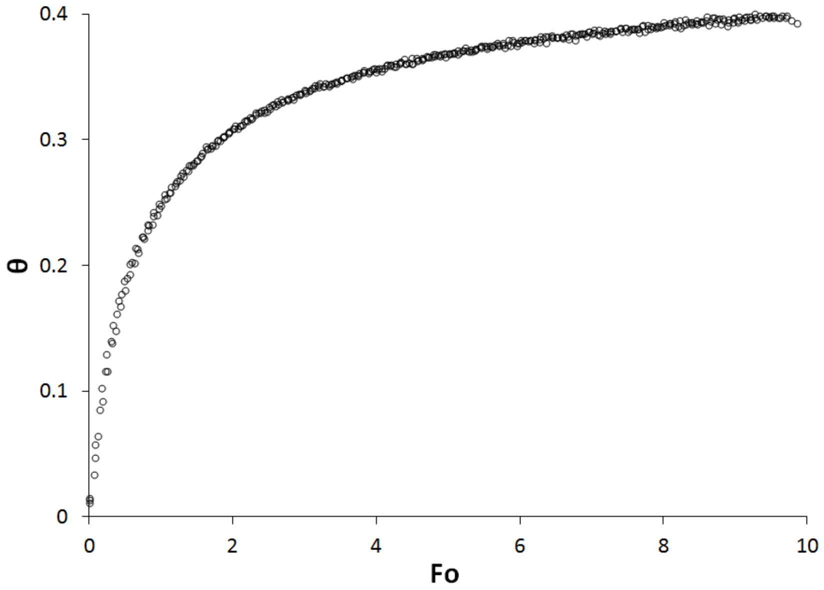

Figure 5.3: Demonstration of $N_2 - O_2$ binary diffusion experiments at 25°C, 50°C, and 70°C collapsing to a single characteristic curve

To extend the analysis to the modified Loschmidt cell, it is proposed that additional parameters diffusibility, Q, and thickness ratio, l^*, be defined as follows:

$$Q = \frac{D_{\text{sample}}}{D_{\text{bulk}}} \tag{5.7}$$

$$l^* = \frac{l}{x_p} \tag{5.8}$$

where D_{sample} is the true diffusivity of the porous sample as compared to the measured value determined by the resistance network method, D_{eff}. The additional variables would be expected to influence concentration profile behaviour such that

$$\theta = \theta\left(x^{*}, \mathrm{Fo}, Q, l^{*}\right) \tag{5.9}$$

Two additional variables now control the characteristic shape of the concentration profile. The applicability of the two additional parameters can be demonstrated by setting up a series of cases where individual variables are varied while the value of the new dimensionless parameters remains constant. Plotting these cases on dimensionless axes should still result in all curves collapsing into a characteristic curve. Table 5.1 lists the case parameters for simulation runs such that all dimensionless parameters are constant. Figure 5.4a shows the data plotted using typical dimensions while Figure 5.4b shows the dimensionless plot.

Table 5.1: Parameters for demonstration of collapsing of curves through dimensionless parameters

Case No.	$D_{\text{bulk}}[\mathrm{m}^2/\mathrm{s}]$	$D_{\text{sample}}[\mathrm{m}^2/\mathrm{s}]$	$l[\mu\mathrm{m}]$	$x_p[\mathrm{mm}]$	$C_{i,b}[\%\mathrm{O}_2]$	$C_{i,t}[\%\mathrm{O}_2]$
1	2.0×10^{-5}	4.0×10^{-6}	300	25.9	100	0
2	1.0×10^{-5}	2.0×10^{-6}	300	25.9	100	0
3	4.0×10^{-5}	8.0×10^{-6}	300	25.9	100	0
4	2.0×10^{-5}	4.0×10^{-6}	600	51.8	100	0
5	2.0×10^{-5}	4.0×10^{-6}	150	12.95	100	0
6	2.0×10^{-5}	4.0×10^{-6}	300	25.9	75	0
7	2.0×10^{-5}	4.0×10^{-6}	300	25.9	100	25
8	1.0×10^{-5}	2.0×10^{-6}	600	51.8	75	25
9	4.0×10^{-5}	8.0×10^{-6}	150	12.95	75	25

The collapsing of the curves is also observable with experimental data for Toray60-Raw and Solvicore Type A GDL. Both GDL's are approximately 200μm thick and have diffusibility in the range of 0.35 to 0.44 [61]. Figure 5.5 shows experimental tests for Toray60-raw and Solvicore Type A GDL's tested in the same Loschmidt cell at 25°C, 50°C, and 70°C.

Previous experimental research has shown that diffusibility of GDL does not vary with temperature [39, 61] and thus the situation shown in Figure 5.5 does approximate constant dimensionless parameters. As such, the six concentration profiles at three different temperatures collapse into one in the same manner as the simulation profiles. The above

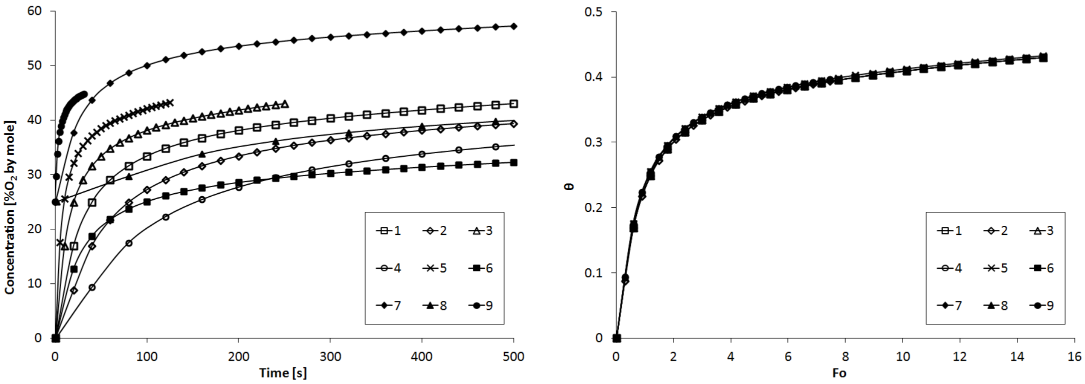

(a) Data plotted on dimensional axes (b) Data plotted on dimensionless axes

Figure 5.4: Demonstration of the applicability of the two new dimensionless variables

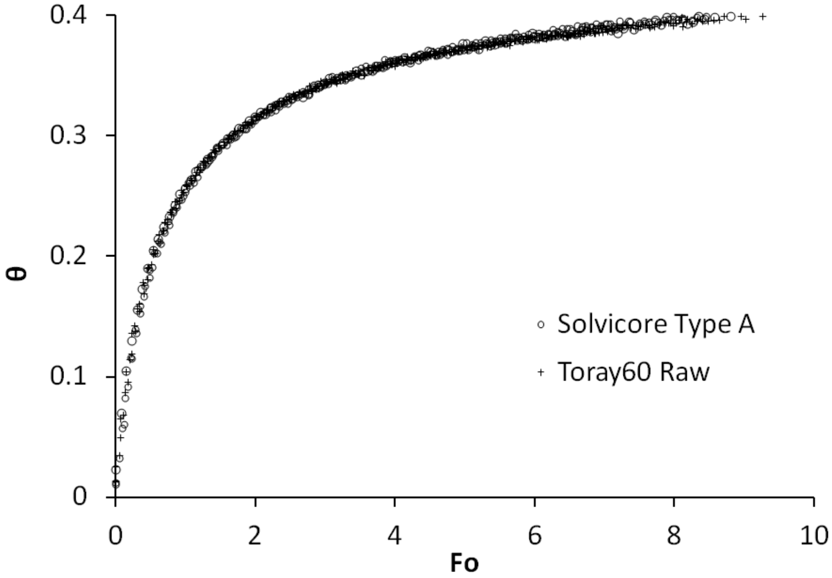

Figure 5.5: Dimensionless plots of experimental concentration profiles for Solvicore and Toray samples at 25°C, 50°C, and 70°C

discussion demonstrates that for a modified Loschmidt cell, when plotting on a $\theta - \mathrm{Fo}$ plot, the only variables have an impact on the shape (and that need to be examined) are diffusibility, Q, and thickness ratio, l^*.

5.3 Parametric Study of Resistance Network Error

This section presents the results of a parametric study on the accuracy of resistance network using the procedure depicted in Figure 4.11. From these results, the source of the error is analysed through examination of the impact of the transience in the modified Loschmidt cell. Transience is examined in terms of unequal flux and gas storage within the calculation domain for the resistance network. A second parametric study simulation study with the same points is performed while extending all simulations beyond the time of greatest transience to show the potential mitigating effects on error. Finally, a generalized uncertainty analysis is performed to show how uncertainty in measured values used to calculate D_{eff} impact the uncertainty of D_{eff}.

The parametric study on the accuracy of the resistance network method investigates the effect of the sample diffusivity and the sample thickness. Since it is only the diffusibility and thickness ratio that control the characteristic curve of the simulation output, the bulk diffusivity and characteristic length were held constant. Bulk diffusivity was set as $2.0 \times 10^{-5}\text{m}^2/\text{s}$ (approximately equal to the $\text{N}_2 - \text{O}_2$ diffusion coefficient at standard temperature and pressure) and a gas probe location of 25.9mm. Each of the experimental test simulations ran for 250s. Figure 5.6 shows the error associated with the resistance network plotted for each sample thickness series over a range of sample diffusivities ranging between 2.0×10^{-5} and $1.0 \times 10^{-7}\text{m}^2/\text{s}$.

The resistance ratio, denoted by Ω^*, is defined as

$$\text{Resistance Ratio} = \Omega^* = \frac{\left(\frac{l}{D_{\text{sample}}}\right)}{\left(\frac{x_p - l}{D_{\text{bulk}}}\right)} = \frac{l^*}{Q\,(1 - l^*)} \tag{5.10}$$

which represents the relative impact of the porous sample and the surrounding bulk gas on the value found for D_{eq}. The resistance ratio, Ω^*, provides the most concise correlation to error of the variables examined. In Figure 5.6, the curves exhibit behaviour in four distinct regions based on the value of the Ω^*. They are as follows:

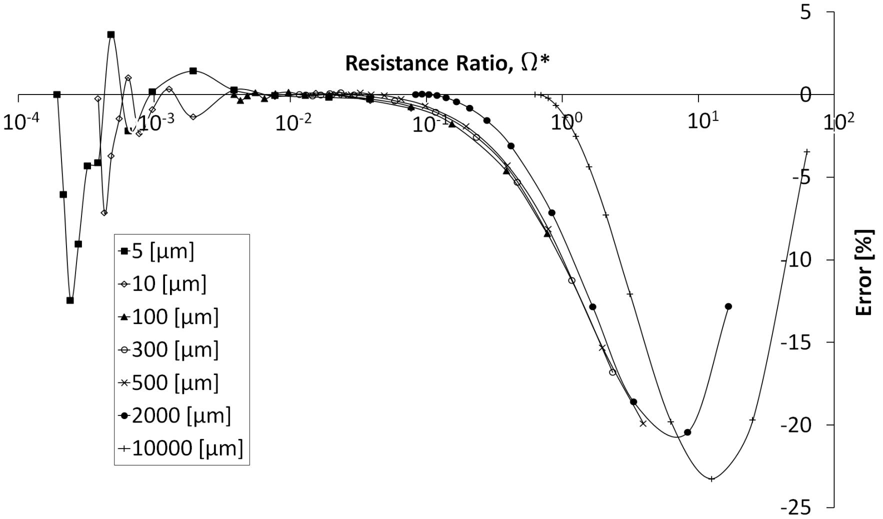

Figure 5.6: Plot of error for various thicknessnes and diffusivities of sample

For $\Omega^* < 0.01$, there is significant instability in the output due to the extremely small value of sample resistance. The D_{eq} found through matching is so similar to D_{bulk} that the small errors due to artifacts related to the simulation or matching algorithm that had previously been negligible become detectable. The magnifications of these small errors is further explained by Section 5.3.2

For $0.01 < \Omega^* < 0.1$, the resistance network approximation gives extremely accurate values for D_{eq} with errors less than 1% such that it is nearly equal to the true value for D_{sample}. This is likely due to the relative resistance of the porous sample being sufficiently small that the concentration-time curve is still nearly the same shape as a case with no sample. The evolution of concentration in the two chambers is still nearly symmetrical.

For $0.1 < \Omega^* < 10$, as the sample becomes increasingly resistant to diffusion, the resistance network method begins to break down and give very significant errors. The porous sample is has a sufficiently large fraction of the total resistance such that the sample of the concentration-time curve has changed measurably. The evolution of concentration in the two chambers is becoming increasingly asymmetric.

For $\Omega^* > 10$, as the resistance of the porous sample begins to dominate the overall resistance, the error of the effective diffusion coefficient become increasingly accurate.

Figure 5.6 shows that the resistance network has the potential to introduce significant errors into the calculation of D_{eff}. However, if the parameters are chosen correctly, it is possible to operate in a Ω^* range that minimizes error originating from application of the resistance network.

5.3.1 Flux Gradient Analysis

To understand the behaviour of the accuracy predicted for the resistance network method shown in Section 5.3, the conflict between the Loschmidt cell's variable flux and the steady-state assumptions of the resistance network is further examined. The discussion looks specifically at the dimensionless form of the concentration profile function shown in Equation 5.6. Taking the derivative of Equation 5.6 with respect to x^* gives

$$\frac{\partial \theta}{\partial x^*} = -\frac{2}{L^*} \sum_{m=0}^{\infty} \left\{ e^{\frac{-(2m+1)^2 \pi^2 Fo}{(L^*)^2}} \cos\left[\frac{(2m+1)\,\pi x^*}{L^*}\right] \right\} \tag{5.11}$$

where the dimensionless concentration gradient is directly proportional to the flux at a specific time and location. Equation 5.11 can be integrated with respect to Fo from zero to Fo to obtain

$$\int_0^{Fo} \frac{\partial \theta}{\partial x^*} dFo = \frac{2}{L^*} \sum_{m=0}^{\infty} \left\{ \frac{\cos\left[\frac{(2m+1)\pi x^*}{L^*}\right]}{\left[\frac{(2m+1)\pi}{L^*}\right]^2} \left[e^{\frac{-(2m+1)^2 \pi^2 Fo}{(L^*)^2}} - 1 \right] \right\} \tag{5.12}$$

which is an expression that is proportional to the cumulative flux past a specific point up until a specific time. The cumulative flux is a useful value since the curve fitting is performed over a period of time beginning from zero when diffusion is first allowed to start. Using a value that retains some history of flux visualize the impact of the curve fitting over a period of time. Figure 5.7a shows a plot of Equation 5.11 at $x^* = 0$, the sliding gate valve, and $x^* = 1$, the probe location, over a range of values for Fo. The two locations coincide with the two edges of the region being calculated for the resistance network. Figure 5.7b shows a plot of Equation 5.12 with increasing Fo, normalized at each time interval based on the maximum cumulative flux at that time. The maximum cumulative flux always occurs at the sliding gate valve since all oxygen passing into the upper chamber must first pass through the center of the apparatus. As oxygen moves further from the center (or the source) it is progressively stored in the volume and the cumulate flux of later sections gradually reduces.

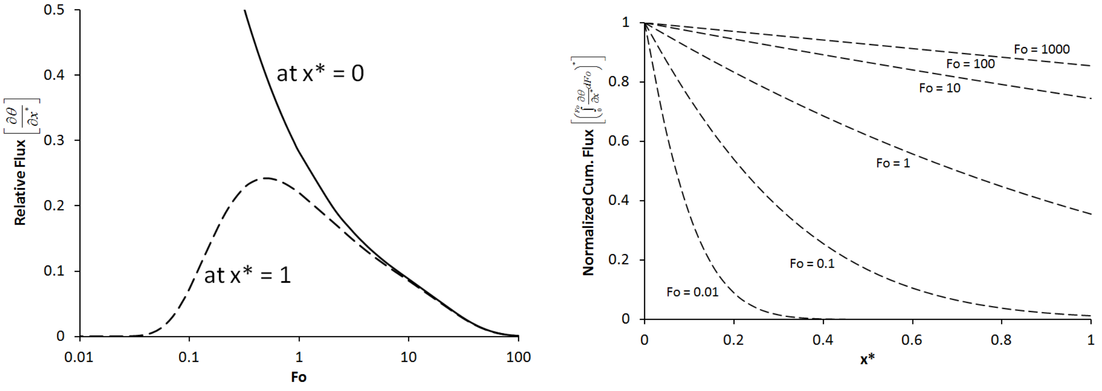

(a) Comparison of relative flux, $\frac{\partial\theta}{\partial x^*}$

(b) Cumulative flux profile over time

Figure 5.7: Comparison of relative flux and cumulative flux within the calculation domain of the resistance network method

In Figure 5.7a, the initial difference in flux between the two locations is extremely large. At small times, the concentration profile still closely resembles the initial stepwise concentration change such that there is an extremely steep gradient near the middle of the apparatus ($x^* = 0$) while the rest of chamber still has nearly zero O_2 concentration and thus a nearly zero concentration gradient. As seen in Figure 4.2a, diffusion eventually brings the concentration gradient throughout the apparatus within the same order of magnitude. Beyond a Fourier number of approximately 10, the flux at the two points becomes nearly equal. When the flux at the inlet and outlet of the resistance network calculation domain are nearly equal, this indicates that the flux in the entire region of $0 < x^* < 1$ is nearly constant. Since Figure 5.7b plots the integral of flux at a point, it shows the total flux that has passed each point if the fitting equation was used to match for a diffusivity. Looking at Figure 5.7b, if matching for a diffusivity was performed at Fo = 0.1, the impact of a sample placed at $x^* = 0.8$ would be nearly undetectable (between 0.03-0.04) due to the extremely small amount of cumulative flux through that region. The plot also shows the straightening of the cumulative flux profile over time. Knowing that the volume per unit length of the chamber is constant, a increasing linearity of the cumulative flux profile indicates that less and less storage of gas will occur. The calculations for the resistance network make no allowances for the storage of gas over time. This becomes an increasing accurate assumption once Fo > 10. From Figures 5.7a and 5.7b it can be understood that at low Fourier numbers, the Loschmidt cell is significantly more transient in terms of relative flux and storage of gas.

The simulations used for the data in Figure 5.6 were run to 250s of test time, which approximately follows the procedure of previous experimental work [57, 39, 59, 53, 58] as well as the experimental data provided throughout this study. For a case with only $\mathrm{N}_2-\mathrm{O}_2$ binary gas diffusion at standard ambient temperature and pressure, 250s would correspond to $\mathrm{Fo} = 7.45$. When a sample is inserted into the apparatus, the additional resistance causes the concentration profile to evolve at a reduced rate. Previously, Fo was an expression of the progress of concentration profile decay. To express progress in the modified Loschmidt cell with a sample, the "equivalent Fourier number", $\mathrm{Fo}_{\mathrm{eq}}$, is introduced and is defined as

$$\mathrm{Fo}_{\mathrm{eq}} = \frac{D_{\mathrm{eq}} t}{x_p^2} \tag{5.13}$$

where D_{eq} is the value obtained from the curve fitting of a Loschmidt cell test with a sample. For a test with a very thick or low diffusivity sample, $\mathrm{Fo}_{\mathrm{eq}}$ can be significantly less than Fo. For example a 500μm thick sample with $D_s = 1.0 \times 10^{-7}\mathrm{m}^2/\mathrm{s}$ has $D_{\mathrm{eq}} = 4.13 \times 10^{-6}\mathrm{m}^2/\mathrm{s}$. This reduces the $\mathrm{Fo}_{\mathrm{eq}}$ to 1.54. While $\mathrm{Fo}_{\mathrm{eq}}$ is only an approximation of the degree of concentration profile decay the reduction of $\mathrm{Fo}_{\mathrm{eq}}$ can be understood as moving the overall Loschmidt cell test further into the unsteady region where relative flux is unequal (Figure 5.7a) and leaving a significant amount of gas storage is required before reaching a steady profile (Figure 5.7b). Another effect of a significant difference between Fo and $\mathrm{Fo}_{\mathrm{eq}}$ is increasing asymmetry between the concentration profile in the upper and lower chambers. With an increasingly resistive sample (and decreasing $\mathrm{Fo}_{\mathrm{eq}}$), the upper chamber profile development is increasing retarded while the lower chamber diffusion progresses unimpeded. This asymmetry of concentration profile is also not accounted for in the resistance network method.

The definition for resistance ratio, Ω^*, in Equation 5.10 can be combined with the definition for equivalent diffusivity, D_{eq}, in Equation 4.5 modified by replacing D_{eff} with D_{sample} to give

$$\frac{x_p}{D_{\mathrm{eq}}} = \left(\frac{x_p - l}{D_{\mathrm{bulk}}}\right)(1 + \Omega^*) \tag{5.14}$$

Substituting in the definitions for Fo and $\mathrm{Fo}_{\mathrm{eq}}$ leads to

$$\frac{\mathrm{Fo}_{\mathrm{eq}}}{\mathrm{Fo}} = \frac{1}{(1 - l^*)(1 + \Omega^*)} \tag{5.15}$$

Equation 5.15 demonstrates the relationship between the Fourier number ratio and the resistance ratio. The data points in Figure 5.6 can be replotted on the the Fourier ratio horizontal axis to give Figure 5.8.

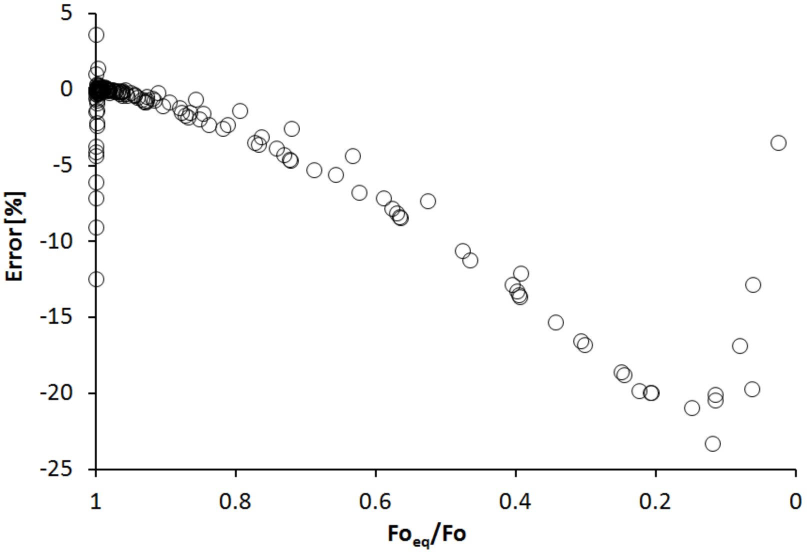

Figure 5.8: Plot of error for all data sets with respect to the relative value between $\mathrm{Fo}_{\mathrm{eq}}$ and Fo

The Fourier number ratio has caused all of the data to collapse almost completely into a single curve and shows that the error has a nearly linear relationship with the Fourier number ratio. The errors at $\mathrm{Fo}_{\mathrm{eq}}/\mathrm{Fo} = 1$ correspond to the error in the region of $\Omega^* < 0.01$ and the error at $\mathrm{Fo}_{\mathrm{eq}}/\mathrm{Fo} = 0$ correspond to the error in the region of $\Omega^* > 10$ from Figure 5.6. The preceding discussion reveals that a fairly significant portion of the error observable for high Ω^* can be attributed to the relatively low $\mathrm{Fo}_{\mathrm{eq}}$ of the simulation runs. Figure 5.8

shows that reducing $\mathrm{Fo_{eq}}$ has a significant impact on the error and requires additional investigation. For illustrative purposes, a sample of 500μm at diffusion coefficients ranging from $1.00 \times 10^{-7}\mathrm{m^2/s}$ to $1.60 \times 10^{-5}\mathrm{m^2/s}$ was simulated to varying time lengths. The thickness of 500μm was selected to enhance the effects of the overall sample resistance from the $100-300\mu$m thickness of typical GDL. Figure 5.9 shows the change of error when fitting to varying $\mathrm{Fo_{eq}}$.

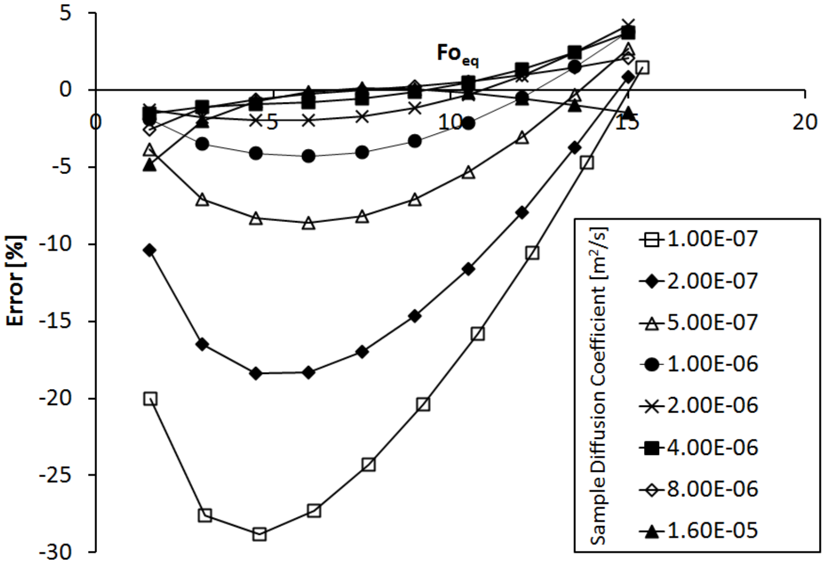

Figure 5.9: The effect of Fourier number on the error of a 500μm thick sample

The results of Figure 5.9 demonstrates that the fitting time has a very significant impact on the error of the resistance network method. The constantly changing error with respect to fitting time is a result of the difference in shape between the analytical equation concentration-time profile and simulation generated time-concentration profile. As the effect of the sample becomes more pronounced, the shape of the curve deviates more and results in a greater maximum error. Selection of a $\mathrm{Fo_{eq}} = 12.5$ can potentially mitigate a significant amount of error shown in Figure 5.6. While each of the curves cross the zero error line at a different value of $\mathrm{Fo_{eq}}$, it is notable that all cross at a value greater than 10. This helps to further demonstrate the previous proposition that the error relates to non-conformity with resistance network assumptions and that after $\mathrm{Fo_{eq}} > 10$, the system becomes significantly closer to steady-state. With the finding that $10 < \mathrm{Fo_{eq}} < 15$ appears to minimize the errors, the same sample diffusion coefficient and thickness simulations seen in Figure 5.6 are recalculated so that each simulation has a duration to give $\mathrm{Fo_{eq}} = 12.5$. Each simulation has an independently determined duration and the simulations with extremely thick or low diffusion coefficients may take over an order of magnitude more time to run. Figure 5.10 shows the error associated when the simulations duration is constrained by $\mathrm{Fo_{eq}} = 12.5$.

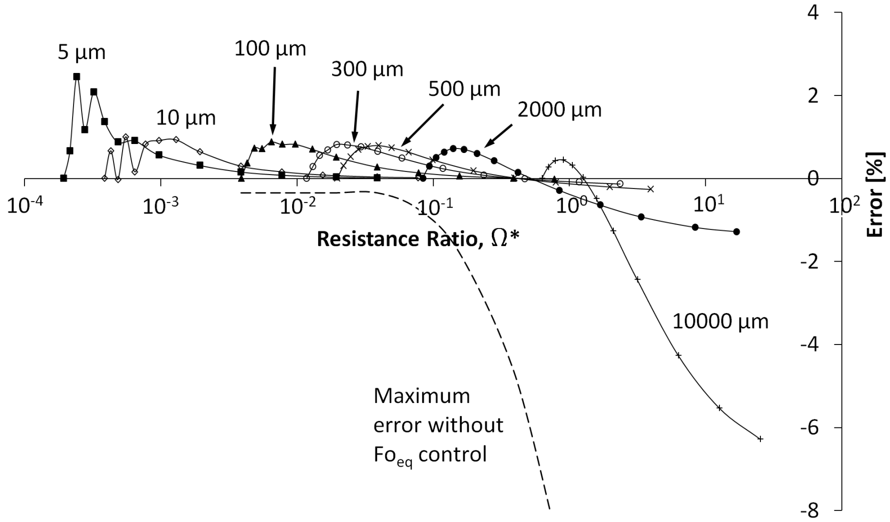

Figure 5.10: Plot of error for various thicknesses and diffusivities of sample where $\mathrm{Fo_{eq}} = 12.5$

As seen in Figure 5.10, controlling of $\mathrm{Fo_{eq}}$ can help to significantly mitigate the error resulting from the resistance network. For all values of thickness and diffusivity (except for 5μm and 10000μm), the error is less than 1%. Even the extreme values of thickness show a very significant decrease in error. Comparison of the data shown in Figure 5.10 with Figure 5.6 shows that there is a significant reduction of error for $\Omega^* > 0.1$ while the effects for $\Omega^* < 0.1$ are negligible. This coincides with the findings in Figure 5.9 where the samples with higher diffusivity (and thus lower Ω^*) are least impacted by changing Fo.

Controlling $\mathrm{Fo_{eq}}$ in actual experimental measurement helps to bring the error of the resistance network down to the same magnitude as the base uncertainty commonly associated with the Loschmidt cell (approximately 2% for a well executed experiment [29]). The values of thickness and diffusivity far exceed the range of materials that would be commonly encountered for testing. The preceding discussion and results provide evidence of the applicability of the resistance network method despite the non-conformance of assumptions and demonstrates the relatively small error when the method is applied correctly.

5.3.2 Magnification of Uncertainty by the Resistance Network

The previous discussion has focused on the error introduced by using the resistance network method during data reduction for modified Loschmidt cell tests. The effective diffusivity, D_{eff}, that the resistance network calculates for a porous sample is based on measurements for x_p, l, D, and D_{eq}. Uncertainty from each of these measurements contributes to the total uncertainty of D_{eff}. Due to the form of Equation 4.6, which describes how to calculate D_{eff}, there is great potential for magnification of uncertainty of the errors associated with these parameters.

The combined impact of uncertainty in the measured values on D_{eff} can be generally expressed as

$$\delta D_{\text{eff}} = \left[\sum_{n=1}^{N} \left(\frac{\partial D_{\text{eff}}}{\partial X_n} \delta X_n \right)^2 \right]^{\frac{1}{2}} \tag{5.16}$$

where δ is the uncertainty of measured or calculated values, X is a measured value, and N is the total number of measured values. The analysis can be greatly simplified by looking at a single measured value uncertainty and its impact on the uncertainty of D_{eff}. Isolation of one measured variable can also seen as a single measurement uncertainty having a significantly larger magnitude making all other uncertainties negligible on in the summation in Equation 5.16. When removing all but one uncertainty, Equation 5.16 simplifies to

$$\delta D_{\text{eff}} = \left| \frac{\partial D_{\text{eff}}}{\partial X_n} \delta X_n \right| \tag{5.17}$$

To aid in understanding, the uncertainties are expressed as a fraction of the full value. Furthermore, the two uncertainty fractions can be related to each other through the "uncertainty magnification factor", η.

$$\eta_{X_n} = \frac{\frac{\delta D_{\text{eff}}}{D_{\text{eff}}}}{\frac{\delta X_n}{X_n}} = \frac{X_n}{D_{\text{eff}}} \left| \frac{\partial D_{\text{eff}}}{\partial X_n} \right| \tag{5.18}$$

the uncertainty magnification factor shows how the relative uncertainty of a measured value propagates to the calculated value. The partial derivative of the expression for D_{eff} in Equation 4.6 can be taken with respect to each of the four measured values in the expression. The dimensionless variables l^* and Q are employed to simplify and generalize the results. The function g is used to replace a commonly recurring expression in the derivations and is defined as

$$g = \frac{D}{D_{\text{eq}}} = 1 + l^* \left(\frac{1}{Q_{\text{eff}}} - 1 \right) \tag{5.19}$$

The η's of the four measured quantities are found to be

$$\eta_l = \eta_{x_p} = \frac{l^* (g-1)}{Q_{\text{eff}} (g - 1 + l^*)^2} \tag{5.20}$$

$$\eta_D = \frac{l^* (1 - l^*)}{Q_{\text{eff}} (g - 1 + l^*)^2} \tag{5.21}$$

$$\eta_{D_{eq}} = \frac{g l^*}{Q_{\text{eff}} (g - 1 + l^*)^2} \tag{5.22}$$

where Q_{eff} is the effective diffusibility calculated through the resistance network (as opposed to the true diffusibility Q which does not contain errors associated with the resistance network). Examination of each of the dimensionless variables reveals the maximum range of possible values

$Q_{\text{eff}} = \frac{D_{\text{eff}}}{D} \leq 1$:

Diffusibility by definition must be less than 1 (a case where the porous material offers no impedance to diffusion)

$l^* = \frac{l}{x_p} \leq 1$:

Thickness ratio, l^*, is a definition based on the resistance network. The geometry is such that the characteristic length must be greater than the thickness of the sample and in general $l^* << 1$

$g = \frac{D}{D_{\text{eq}}} \geq 1$**:**

Knowing that $D_{\text{eff}} \leq D_{\text{eq}} \leq D$ means that $g \geq \frac{1}{Q_{\text{eff}}}$

The η values can also be plotted with respect to the resistance ratio, Ω^* to understand their impact in the context of the previous section. As seen in Equation 5.10, Ω^* is also expressible in terms of diffusibility and thickness ratio. Figures 5.11 to 5.13 show plots of the magnification factor over a range of resistance ratios when the equations are provided with $0.001 \geq Q_{\text{eff}} \geq 1$ and $0.0002 \geq l^* \geq 0.8$. Each of the points in Figures 5.11 to 5.13 represents a discrete Q_{eff} and l^* point within the range. Maximum Q_{eff} is limited to 1 (equal to diffusibility of bulk gas) and while the minimum was selected as nearly impermeable (1/1000 the diffusivity of bulk gas). With a diffusion length of 25.9mm, the l^* range would span from the thinnest catalyst layer (5μm) up to 20mm.

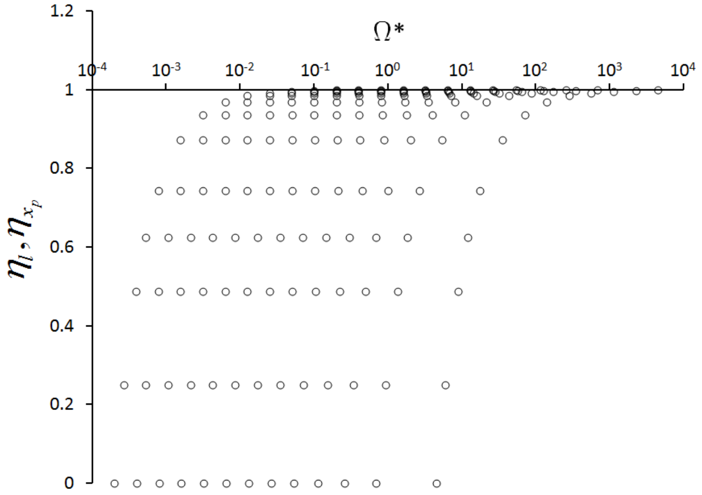

Figure 5.11: Uncertainty magnification factor from measurements of sample thickness, η_l, and characteristic length, η_{x_p}, to D_{eff}

The Ω^* values for Figure 5.11 are expressed on a logarithmic scale. The figure shows that η_l (as well as η_{x_p}) is bounded between 0 and 1. This means that at most the uncertainty of both the sample thickness measurement and the diffusion length measurement have the same relative impact on D_{eff}. Examination of the numerator in Equation 5.20 show that $\eta_l \to 0$ as $g \to 1$. From the expression for g in Equation 5.19, this can be seen to occur when $Q_{\text{eff}} \to 1$ (or $D_{\text{eff}} \to D$). This shows that the effect of uncertainty in the length based measurements have reduced effect as the porous sample's diffusion coefficient becomes less different from the surrounding gas. The figure shows groups of similarly shaped curves beginning at 0 and ending at 1. Each of the curves corresponds to a single discrete l^*.

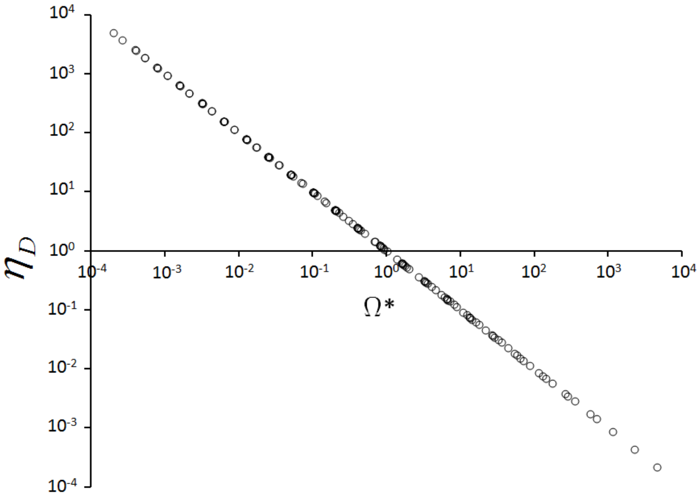

Figure 5.12: Uncertainty magnification factor from measurements of bulk diffusivity, η_D, to D_{eff}

Both the horizontal and vertical axis for η_D in Figure 5.12 are plotted on a logarithmic scale and shows that the magnification factor is linear on a log-log scale. Unlike Figure 5.11, all data sets in Figure 5.12 are collapsed into a single line regardless of Q_{eff} and l^*. It also shows that for $\Omega^* > 1$, the uncertainty is significantly reduced while when $\Omega^* < 1$, there is potential for the uncertainty to be magnified by several orders of magnitude.

Figure 5.13 shows that $\eta_{D_{\text{eq}}}$ has nearly identical behaviour as η_D for $\Omega^* > 1$. Unlike for η_D, the minimum value for the $\eta_{D_{\text{eq}}}$ is 1. This is due to the unique term in the numerator of Equation 5.22 being g which itself has a minimum value of 1. This is an unfortunate results as it indicates that any uncertainty in the value for D_{eq} will at best be directly transferred to D_{eff} and at worst multiplied by several orders of magnitude. This analysis shows that appropriate design of experimental apparatus is required to avoid such large uncertainty. A poorly chosen resistance ratio, Ω^*, can result in the uncertainty overshadowing all other error effects and render the measurements unusable.

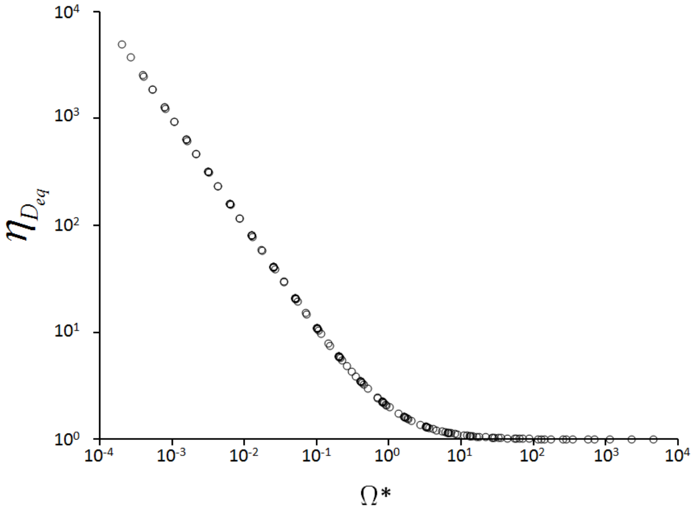

Figure 5.13: Uncertainty magnification factor from measurements of equivalent diffusivity, $\eta_{D_{\mathrm{eq}}}$, to D_{eff}

The thickness and length measurements are inherently less susceptible to uncertainty and the above discussion has shown that their effects are mitigated when calculating the effective diffusion coefficient of the porous sample, D_{eff}. On the other hand, uncertainty for bulk gas diffusion coefficient, D, and the equivalent diffusion coefficient, D_{eq}, measured by the modified Loschmdit cell are significantly magnified when Ω^* is low. In many experimental studies, the value for D is measured directly only for verification while the actual value employed in the calculations are well established literature values for the binary diffusion coefficient. In this way, the primary source of error in most instances are linked to D_{eq}. Assuming that the D_{eq} dominates the uncertainty, Figure 5.13 shows that a $\Omega^* > 1$ is desirable to minimize the magnification of uncertainty when calculating D_{eff}.

Some experiments in literature measured the effective diffusion coefficient of a thin layer deposited on a porous substrate. In this case, measurements must be made for the bulk gas diffusion coefficient, the equivalent diffusion coefficient of the substrate only, and the equivalent diffusion coefficient of the substrate and deposited layer. Figure 5.14 shows a schematic of the resistance network for a situation with a layer deposited on the substrate.

The first step in the resistance network calculations(on the left side of Figure 5.14) is to find the effective diffusion coefficient of the composite porous media (porous substrate

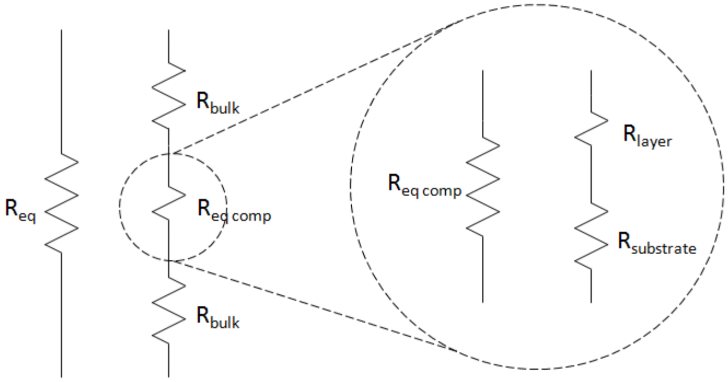

Figure 5.14: Schematic of the two step resistance network used to calculate the diffusivity of a porous layer supported by a substrate

and deposited layer).

$$D_{\text{eq,comp}} = \frac{l_{\text{layer}} + l_{\text{substrate}}}{\frac{x_p}{D_{\text{eq}}} - \frac{x_p - l_{\text{layer}} - l_{\text{substrate}}}{D_{\text{bulk}}}} \tag{5.23}$$

The second step uses the values of the composite effective diffusion coefficient and the effective diffusion coefficient of the substrate to find effective diffusion coefficient of the deposited layer.

$$D_{\text{layer}} = \frac{l_{\text{layer}}}{\frac{l_{\text{layer}} + l_{\text{substrate}}}{D_{\text{eq,comp}}} - \frac{l_{\text{substrate}}}{D_{\text{substrate}}}} \tag{5.24}$$

where l_{layer} is the thickness of the deposited layer, $l_{\text{substrate}}$ is the thickness of the substrate, $D_{\text{eq,comp}}$ is the equivalent diffusion coefficient measured by the Loschmidt cell for the composite substrate and deposited layer, $D_{\text{substrate}}$ is the calculated effective diffusion coefficient of the substrate, and D_{layer} is the calculated effective diffusion coefficient of the deposited layer. The steps outlined above show that $D_{\text{eq,comp}}$ and $D_{\text{substrate}}$, the values used to calculate D_{layer}, already have uncertainty magnified from the original measurements. These uncertainties are magnified a second time when calculating for D_{layer}. Thus is it even more critical to ensure a resistance ratio of 1 or greater at both stages when designing the experiment.

5.3.3 Application to Experimental Studies

Using the above findings, the error contribution of the resistance network can be found for experimental data obtained using the modified Loschmidt cell. Rohling et al. was the first to make measurements using a modified Loschmidt cell and measured four stacked GDL samples in a $CO_2 - O_2$ binary mixture [53]. Astrath et al. compared the measured diffusivity through precisely perforated stainless steel films with simulated values to examine the accuracy of the modified Loschmidt cell [57]. Zamel et al. studied the effect of temperature and additional surface treatment on diffusivity of GDL [39]. Shen et al. measured diffusivity through various thickness catalyst layers deposited on a porous substrate [58] while Chan et al. measured the diffusivity of microporous layers deposited onto a GDL substrate as well as examined the effects of surface treatment [59]. All of the studies used the infinite length approximation and have experiment lengths of $200 - 300$s. Figure 5.15 shows the approximation of experimental error from the five studies plotted with respect to Ω^*.

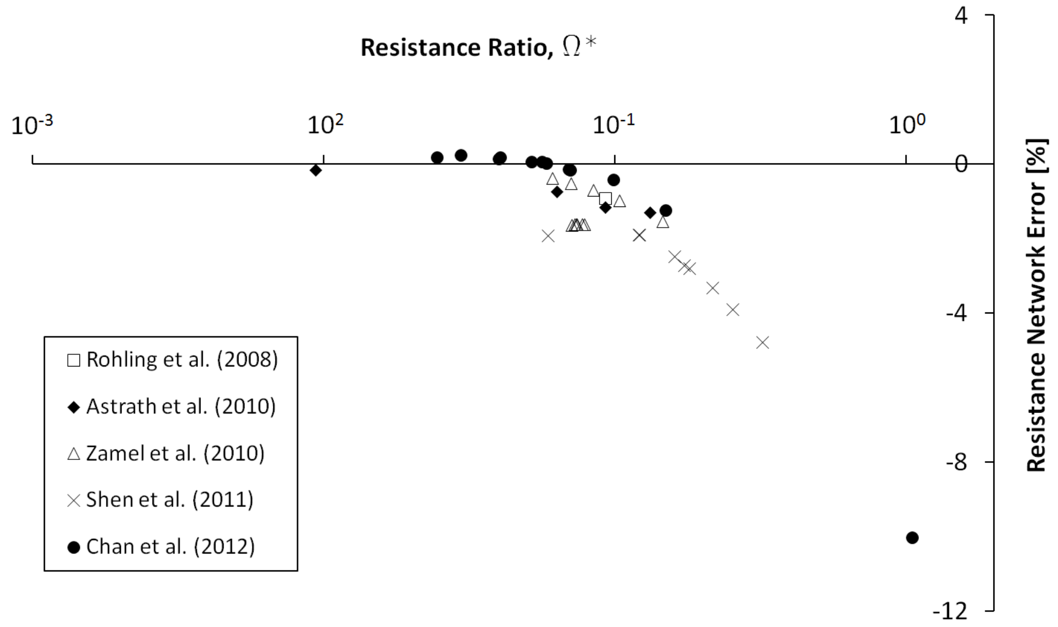

Figure 5.15: Resistance network error approximation for experimental work in literature

The results summarized in Figure 5.15 show that previous experimental studies have resistance ratios ranging between 0.01 and 1. In this range, even without control of Fo_{eq}, the estimated error never exceeds 10%. However, the uncertainty magnification for D_{eq} (from Section 5.3.2) is in the range between 2 and 100. With 2% uncertainty associated with a well executed Loschmidt cell diffusivity measurement [29], the approximate uncertainty in D_{eff} ranges between 200% at $\Omega^* = 0.01$ and 4% at $\Omega^* = 1$. This extreme level of uncertainty is introduced through the calculations of the resistance network and render many results unusable.

Error and uncertainty can be introduced in three separate ways during measurement of the effective diffusion coefficient.

1. Concentration measurement over time (in C and t)
2. Fitting of an analytical equation to the $C - t$ curves to obtain D_{eq}
3. Resistance network calculations to obtain D_{eff}

The first two sources of error and uncertainty are usually controlled by using precision equipment and using appropriate analytical fitting equations. This study shows that the step of calculating D_{eff} has the potential to introduce a significant error and magnify the uncertainty to a degree where it overshadows all other effects. In order to optimize the error and uncertainty introduced by the resistance network method, experimental studies must target a resistance ratio between 1 and 2 with an overall duration resulting in $Fo_{\text{eq}} = 12.5$. The resistance ratio may be manipulated by either reducing the probe distance, x_p, or increasing the sample thickness, l, by stacking multiple layers.

Chapter 6

Concluding Remarks

6.1 Conclusions

In this study, a one-dimensional diffusion simulation was developed to accurately calculate diffusion of gas in a modified Loschmidt cell with a porous sample. Previous studies involving the modified Loschmidt cell converts the diffusion distances within the cell into diffusive resistance, known as the resistance network method, to calculate the effective diffusion coefficient, D_{eff}, of the porous sample. Using the one-dimensional simulation, the error originating from the resistance network method could be isolated and quantified.

The process in both the conventional and modified Loschmidt cell were investigated using dimensionless variables. Dimensionless variables revealed that the behaviour of the conventional Loschmidt cell is dependent only on dimensionless distance, x^*, and dimensionless time, Fo. The modified Loschmidt cell is dependent on the additional variables of thickness ratio, l^*, and diffusibility, Q. The concentration is expressed as dimensionless concentration, θ. With the dimensionless distance being constant (since the O_2 probe location is constant) and the vertical and horizontal axes being θ and Fo, respectively, all dimensionlessly plotted conventional Loschmidt cell tests collapse into a single characteristic curve. For the modified Loschmidt cell, tests plotted dimensionlessly also collapse into a single characteristic curve provided l^* and Q are constant among the tests. The analysis allowed the parametric study of variables that influence resistance network error to examine fewer variables.

The error due to the resistance network was found to vary with resistance ratio, Ω^*. At $\Omega^* < 0.1$, the error for all cases is below 2% and considered negligible. When $\Omega^* > 0.1$, the error increases dramatically with increasing Ω^* up to a maximum of about 20%. Examination of the impact of Fo of the simulation runs and introduction of the equivalent Fourier number, $\mathrm{Fo_{eq}}$, helped to explain and mitigate the error. The analytical fitting equation and resistance network used in the data reduction process are based on steady-state assumptions to which the Loschmidt cell does not conform. While Fo is an expression of "how far along" a conventional Loschmidt cell experiment in terms of diffusion towards steady-state, the addition of a porous sample in the modified Loschmidt cell is an additional impedance to the maturation of the concentration profile and requires the introduction of $\mathrm{Fo_{eq}}$ as an approximate expression progression towards steady-state. By ensuring that an experiment has sufficient time length to ensure that $\mathrm{Fo_{eq}} \approx 12.5$ (thus ensuring that the experiment has nearly reached steady-state), the error of the resistance network is reduced to approximately 1% for most conditions and less than 6% for extremely thick and resistive porous samples.

The resistance network involves using two measured diffusion coefficients, a sample thickness measurement, and the apparatus diffusion length to calculate the effective diffusion coefficient of the porous sample. The uncertainty from the four measured values all have an impact on the uncertainty of D_{eff}. When looking at relative uncertainties (or percentage uncertainty), the uncertainty magnification factor, η was introduced to express how the uncertainty of a single measured value is transferred to D_{eff}. For both the diffusion length and sample thickness measurements, η was found to be always less than or equal to 1. The two diffusion coefficient measurements have extremely high η when $\Omega^* > 1$. For both diffusion coefficient values, η reduces with increasing Ω^* with η_D approaching 0 and $\eta_{D_{\text{eq}}}$ approaching 1 as $\Omega^* \to \infty$. The extremely large value of η_D and $\eta_{D_{\text{eq}}}$ at low Ω^* means a 2% uncertainty in the measured diffusion coefficients (considered the accuracy limit for a Loschmidt cell) can easily be magnified in D_{eff} by one or two orders of magnitude. To avoid significant uncertainty, the experiment should be designed to have $\Omega^* > 1$. Further, this means that $\mathrm{Fo_{eq}}$ of the experiment must be controlled to mitigate errors originating from the resistance network.

6.2 Recommendations

This thesis looked at the error and uncertainty related to the application of the resistance network method in the modified Loschmidt cell. The findings of this study can be applied to the design and construction of modified Loschmidt cell experimental apparatus and procedures to help mitigate uncertainty and error in the final result. The recommendations are as follows:

1. The maximum flow rate of the mass flow controllers for the two gases can be significantly higher than the 100mL/min used by the in-house apparatus. The higher flow rate will allow for a faster and higher purity purge for the initialization of the apparatus. Further, the calibration of the oxygen probe is based on accurate ratios of gases rather than accurate absolute flow rates. Therefore, even though higher flow rate mass flow controllers may have less absolute accuracy and precision, the calibration will be unaffected as long as percentage accuracy and precision are unchanged.

2. The data reduction procedure should use the finite length analytical solution to Fick's law to curve match the experimental results. Use of the finite length solution allows for an unrestricted duration to the experiment as well as reducing error and uncertainty in the Loschmidt cell results. Accuracy and precision in the Loschmidt cell measurement of diffusion coefficients is especially important due to the propensity for uncertainty to be magnified when applying the resistance network method.

3. The resistance ratio for experiments should be approximately 1. For cases of measurement of the diffusion coefficient of a porous layer deposited on a substrate, the resistance ratio between the deposited layer and substrate should be approximately 1 while at the same time the resistance ratio between the two separate layers and the remaining bulk gas should also be approximately 1. There is some difficulty since the actual diffusion coefficients of the measured substances are unknown however analytical correlations for diffusion coefficient are sufficiently accurate to give estimates within one order of magnitude. A resistance ratio of 1 helps ensure that the uncertainty magnification is closer to 1 while the error from the resistance network method is minimized.

4. The duration of the experiments should be set based on trying to reach $\mathrm{Fo}_{\mathrm{eq}} = 12.5$. In order to do so, an estimate must be made for D_{eff}. Proper control of the experiment

duration can significantly mitigate the error resulting from the use of the resistance network method.

APPENDICES

Appendix A

Analytical Equation Derivation

A.1 Finite Length Derivation

The analytical equation for the concentration-time profile for the conventional Loschmidt cell can be derived by applying the appropriate boundary conditions to Fick's law in one dimension. Previous studies reference both Crank [8] and Carslaw [27] for the final equation however neither book presents the derivation or final result for this exact situation. Both authors do present similar cases and examples of how a solution could be approached.

Beginning with partial differential equation (PDE) describing Fick's law in one dimension

$$\frac{\partial C}{\partial t} = D\frac{\partial^2 C}{\partial x^2} \tag{A.1}$$

With the boundary condition (BC) and initial conditions (IC's) for the Loschmidt cell

$$\left(\frac{\partial C}{\partial x}\right)_{x=\pm\frac{L}{2}} = 0 \tag{A.2}$$

$$C\left(-\frac{L}{2} < x < 0\right) = C_{o,b} \tag{A.3}$$

$$C\left(0 < x < \frac{L}{2}\right) = C_{0,t} \tag{A.4}$$

Applying the method of separation of variables, the function for concentration is assumed to be expressible as the product of two functions each with only one variable

$$C\left(x, t\right) = \phi(x)\tau(t) \tag{A.5}$$

Substitution of the assumption of separability into the PDE and boundary condition yields

$$\frac{1}{\tau D}\frac{d\tau}{dt} = \frac{1}{\phi}\frac{d^2\phi}{dx^2} \tag{A.6}$$

The separation of variables in Equation A.6 causes the left and right sides to be functions with respect to only t and x, respectively. For this to be true for all t and x, the both sides must equal some constant value, set as k. The PDE can then be expressed as two ordinary differential equations (ODE's)

$$\frac{d\tau}{dt} - kD\tau = 0 \tag{A.7}$$

$$\frac{d^2\phi}{dx^2} - k\phi = 0 \tag{A.8}$$

The BC is also expressible in terms of the new functions

$$\left(\frac{d\phi}{dx}\right)_{x=\pm\frac{L}{2}} = 0 \tag{A.9}$$

The solution to Equation A.8 is found by examining $k = \lambda^2, 0, -\lambda^2$ as the three possible solutions which are summed due to super-positioning

$$\phi\left(x\right) = \left[Ae^{\lambda x} - Be^{-\lambda x}\right] + \left[Cx + D\right] + \left[E\cos\left(\lambda x\right) + F\sin\left(\lambda x\right)\right] \tag{A.10}$$

where A through F are unknown constants. Substitution of the BC's gives a infinite set of values and eigenfunctions that satisfy the conditions

$$\phi_m(x) = F_m \sin(\lambda_m x) + D \tag{A.11}$$

where the eigenvalues are defined as

$$\lambda_m = \frac{(2m+1)\pi}{L}, m = 0, 1, 2, \ldots \tag{A.12}$$

The eigenvalues are then used to solve the time dependent equation of the separation of variables. The results are

$$\tau_m = G_m e^{\frac{-(2m+1)\pi^2 Dt}{L^2}} \tag{A.13}$$

This leads to the combined solution of

$$C(x,t) = \sum_{m=0}^{\infty} \left\{ H_m e^{-\frac{(2m+1)\pi^2 Dt}{L^2}} \sin\left[\frac{(2m+1)\pi x}{L}\right] + I_m \right\} \tag{A.14}$$

To apply the initial conditions, the stepwise change in concentration can be expressed as a square sinusoidal wave. The expressions for a square sinusoid with a maximum value of $C_{o,b}$, a minimum value of $C_{o,t}$, and a frequency of $\frac{1}{2L}$ is

$$C(x) = \frac{C_{o,b} + C_{o,t}}{2} + (C_{o,b} - C_{o,t}) \frac{2}{\pi} \sum_{m=0}^{\infty} \left\{ \frac{\sin\left[\frac{(2m+1)\pi x}{L}\right]}{2m+1} \right\} \tag{A.15}$$

The very similar form between Equation A.14 and A.15 allows for a very easy substitution and the final solution of

$$C(x,t) = \frac{C_{o,b} + C_{o,t}}{2} + (C_{o,b} - C_{o,t}) \frac{2}{\pi} \sum_{m=0}^{\infty} \left\{ \frac{e^{\frac{-(2m+1)\pi^2 Dt}{L^2}}}{2m+1} \sin\left[\frac{(2m+1)\pi x}{L}\right] \right\} \tag{A.16}$$

References

[1] Jang JH, mon Yan W, Shih CC. Effects of the gas diffusion-layer parameters on cell performance of PEM fuel cells. *Journal of Power Sources*. 2006;161(1):323–332.

[2] Spiegel C. *PEM Fuel Cell Modeling and Simulation Using MATLAB*. Elsevier Academic Press. 2008.

[3] Barbir F. *PEM Fuel Cells: Theory and Practice*. Burlington, Massachusetts: Elsevier Academic Press. 2005.

[4] Lim C, CYWang. Effects of hydrophobic polymer content in GDL on power performance of a PEM fuel cell. *Electrochimica Acta*. 2004;49:4149–4156.

[5] Williams MV, Begg E, Bonville L, Kunz HR, Fenton JM. Characterization of gas diffusion layers for PEMFC. *Journal of The Electrochemcial Society*. 2004;151(8):A1173–A1180.

[6] Zhang H, Wang X, Zhang J, Zhang J. *PEM Fuel Cell Electrocatalysts and Catalyst Layers*, chap. Conventional Catalyst Ink, Catalyst Layer and MEA Preparation. Springer. 2008;.

[7] Shen PK. *PEM Fuel Cell Electrocatalysts and Catalyst Layers*, chap. PEM Fuel Cell Catalyst Layers and MEAs. Springer. 2008;.

[8] Crank J. *The Mathematics of Diffusion*. Bristol, England: Oxford University Press, 2nd ed. 1975.

[9] Yuan XZ, Wang H. *PEM Fuel Cell Electrocatalysts and Catalyst Layers*, chap. PEM Fuel Cell Fundamentals. Springer. 2008;.

[10] Pasaogullari U, Wang CY. Two-phase transport and the role of micro-porous layer in polymer electrolyte fuel cells. *Electrochimica Acta*. 2004;49(25):4359–4369.

[11] Qi Z, Kaufman A. Imprvement of water management by a microporous sublayer for PEM fuel cells. *Journal of Power Sources*. 2002;109(1):38–46.

[12] Giorgi L, Antolini E, Pozio A, Passalacqua E. Influence of the PTFE content in the diffusion layer in low-Pt loading electrodes for polymer electrolyte fuel cells. *Electrochimica Acta*. 1998;43(24):3675–3680.

[13] Ramasamy RP, Kumbur EC, Mencha MM, Liu W, Moore D, Murthy M. Investigation of macro- and micro-porous layer interaction in polymer electrolyte fuel cells. *International Journal of Hydrogen Energy*. 2008;33(13):3351–3367.

[14] Uchida M, Aoyama Y, Eda N, Ohta A. New preparation method for polymer-electrolyte fuel cells. *Journal of The Electrochemical Society*. 1995;142(2).

[15] Uchida M, Aoyama Y, Eda N, Ohta A. Investigation of the microstructure in the catalyst layer and effects of both perfluorosulfonate ionomer and PTFE-loaded carbon on the catalyst layer of polymer electrolyte fuel cells. *Journal of The Electrochemical Society*. 1995;142(12).

[16] Cho YH, Yoo SJ, Cho YH, Park HS, Park IS, Lee JK, Sung YE. Enhanced performance and improved interfacial properties of polymer electrolyte membrane fuel cells fabricated using sputter-desposited Pt thin layers. *Electrochimica Acta*. 2008; 53:6111–6116.

[17] Hsu C, Wan C. An innovative process for PEMFC electrodes using the expansion of Nafion film. *Journal of Power Sources*. 2003;115:268–273.

[18] Wilson MS, Gottesfeld S. High performance catalyzed membranes of ultra-low Pt loadings for polymer electrolyte fuel cells. *Journal of The Electrochemical Society*. 1992;139(2).

[19] Taylor AD, Kim EY, Humes VP, Kizuka J, Thompson LT. Inkjet printing of carbon supported platinum 3-D catalyst layers for use in fuel cells. *Journal of Power Sources*. 2007;171:101–106.

[20] Maric R. *PEM Fuel Cell Electrocatalysts and Catalyst Layers*, chap. Spray-based and CVD processes for synthesis of fuel cell catalysts and thin catalyst layers. Springer. 2008;.

[21] Ticianelli E, Derouin C, Redondo A, Srinivasan S. Methods to advance technology of proton exchange membrane fuel cells. *Journal of The Electrochemical Society*. 1988; 135(9).

[22] Kumar GS, Raja M, Parthasarathy S. High performance electrodes with very low platinum loading for polymer electrolyte fuel cells. *Electrochimica Acta*. 1995;40(3):285–290.

[23] Chapman S. *The Mathematical Theory of Non-Uniform Gases.* New York, NY: Cambridge University Press, 3rd ed. 1970.

[24] Poling BE, Prausnitz JM, O'Connell JP. *The Properties of Gases and Liquids.* New York, NY: McGraw-Hill, 5th ed. 2001.

[25] Incropera FP, Dewitt DP, Bergman TL, Lavine AS. *Fundamentals of Heat and Mass Transfer.* Danvers, MA: John Wiley and Sons, 6th ed. 2007.

[26] Nagle RK, Saff EB, Snider AD. *Fundamentals of Differential Equations and Boundary Value Problems.* Pearson, 4th ed. 2004.

[27] Carslaw H, JCJaeger. *Conduction of Heat in Solids.* London: Oxford, 2nd ed. 1959.

[28] Cussler EL. *Multicomponent Diffusion.* Elsevier. 1976.

[29] Marrero T, Mason E. Gaseous Diffusion Coefficients. *Journal of Physical and Chemical Reference Data*. 1972;1(1):3–118.

[30] Demirel Y. *Nonequilibirum Thermodynamics.* Amsterdam, The Netherlands: Elsevier, 2nd ed. 2007.

[31] Dullien FAL. *Porous Media.* San Diego, CA: Academic Press, 2nd ed. 1992.

[32] Satterfield CN, Sherwood TK. *The Role of Diffusion in Catalysis.* Reading, MA: Addison-Wesley. 1963.

[33] Bruggeman D. Calculation of various physical constants in heterogenous substances I: dielectric constants and conductivity of mixed bodies from isotropic substances. *Annalen der Physik.* 1935;24():636–664.

[34] Nader GNW. Prediction of transport processes within porous media: diffusive flow processes within a homogeneous swarm of spherical particles. *AIChE Journal.* 1973; 19:112–119.

[35] Tomadakis M, Sotirchos S. Ordinary and transition regime diffusion in random fiber structures. *AIChE Journal.* 1993;39:397–412.

[36] Nam J, Kaviany M. Effective diffusivity and water-saturation distribution in single and two-layer PEMFC diffusion medium. *International Journal of Heat and Mass Transfer.* 2003;46:4595–4611.

[37] Das P, Li X, Liu Z. Effective transport coefficients in PEM fuel cell catalyst and gas diffusion layers: Beyond Bruggeman approximation. *Applied Energy.* 2009;.

[38] Zamel N, Li X, Shen J. Correlation for the Effective Gas Diffusion Coefficient in Carbon Paper Diffusion Media. *Energy Fuels.* 2009;23:6070–6078.

[39] Zamel N, Astrath NG, Li X, Shen J, Zhou J, Astrath FB, Wang H, Liu ZS. Experimental measurement of effective diffusion coefficient of oxygen-nitrogen mixture in PEM fuel cell diffusion media. *Chemical Engineering Science.* 2010;65:931–937.

[40] Mason E, Malinauskas A. *Gas Transport in Porous Media: The Dusty Gas Model.* Elsevier. 1983.

[41] Hirschfelder JO, Curtiss CF, Bird RB. *Molecular Theory of Gases and Liquids.* New York, NY: Wiley and Sons. 1954.

[42] Prausnitz JM, Benson PR. Effective collision diameters and correlation of some thermodynamic properties of solutions. *AlChE Journal.* 2004;5(3):301–303.

[43] Baker D, Wieser C, Neyerlin K, Murphy M. The Use of Limiting Current Density to Determine Transport Resistance in PEM Fuel Cells. *ECS Transactions.* 2006;3:989–999.

[44] Baker D, Caulk D, Neyerlin K, Murphy M. Measurement of Oxygen Transport Resistance in PEM Fuel Cells by Limiting Current Method. *Journal of the Electrochemical Society*. 2009;156:B991–B1003.

[45] Beuscher U. Experimental Method to Determine the Mass Transport Resistance of a Polymer Electrolyte Fuel Cell. *Journal of The Electrochemical Society*. 2006; 153:A1788–A1793.

[46] Stumper J, Haas H, Granados A. In Situ Determination of MEA Resistance and Electrode Diffusivity of a Fuel Cell. *Journal of The Electrochemical Society*. 2005; 152:A837–A844.

[47] Kramer D, Freunberger S, Flükiger R, Schneider I, Wokaun A, Büchi F, Scherer G. Electrochemical diffusimetry of fuel cell gas diffusion layers. *Journal of Electroanalytical Chemistry*. 2008;612:63–77.

[48] Flückiger R, Freunberger S, Kramer D, Wokaun A, Scherer G, Büchi F. Anisotropic effective diffusivity of porous gas diffusion layer materials for PEFC. *Electrochimica Acta*. 2008;54:551–559.

[49] Becker J, Flückiger R, Reum M, Büchi F, Marone F, Stampanoni M. Determination of Material Properties of Gas Diffusion Layers: Experiments and Simulations Using PHase Contrast Tomographic Microscopy. *Journal of The Electrochemical Society*. 2009;156:B1175–B1181.

[50] Martínez M, Shimpalee S, Zee JV. Measurement of MacMullin Numbers for PEMFC Gas-Diffusion Media. *Journal of The Electrochemcial Society*. 2009;156:B80–B85.

[51] Martínez-Rodríguez M, Tong C, Shimpalee S, Zee JV. Characterization of Microporous Layer in Carbon Paper GDL for PEM Fuel Cell. *ECS Transactions*. 2010; 33:1133–1141.

[52] LaManna J, Kandlikar S. Determination of effective water vapor diffusion coefficient in pemfc gas diffusion layers. *International Journal of Hydrogen Energy*. 2011;36:5021–5029.

[53] Rohling J, Shen J, Zhou J, Gu C. Photothermal deflection measurement of effective gas diffusion coefficient of a porous medium. *The European Physical Journal Special Topics*. 2008;153:111–113.

[54] Rohling J, Shen J, Wang C, Zhou J, Gu C. Determination of binary diffusion coefficient of gases using photothermal deflection technique. *Applied Physics B*. 2008;87:355–362.

[55] Zhang F, Hayes R, Kolaczkowski S. A new technique to measure the effective diffusivity in a catalytic monolith washcoat. *Chemical Engineering Research and Design*. 2004;82(A4):481–489.

[56] Yovanovich MM. Advanced Heat Conduction. 1993. University of Waterloo.

[57] Astrath N, Shen J, Astrath F, Zhou J, Huang C, Yuan X, Wang H, Navessin T, Liu Z, Vlanjnic G, Bessarabov D, Zhao X. Determination of effective gas diffusion coefficients of stainless steel films with differently shaped holes using a Loschmidt diffusion cell. *Review of Scientific Instruments*. 2010;81:046104.

[58] Shen J, Zhou J, Astrath NG, Navessin T, Liu ZSS, Lei C, Rohling JH, Bessarabov D, Ye SKS. Measurement of effective gas diffusion coefficients of catalyst layers of PEM fuel cells with Loschmidt diffusion cell. *Journal of Power Sources*. 2011;196:674–678.

[59] Chan C, Zamel N, Li X, Shen J. Experimental measurement of effective diffusion coefficient of gas diffusion layer/microporous layer in PEM fuel cells. *Electrochimica Acta*. 2012;65:13–21.

[60] Fuller E, Schettler P, Giddings J. New method for prediction of binary gas phase diffusion coefficients. *Industrial and Engineering Chemistry*. 1966;58:19–27.

[61] Unsworth G, Dong L, Li X. Investigation of Oxygen-Nitrogen Gas Diffusion in PEMFC Porous Media Using a Loschmidt Cell. *AIChE Journal*. 2012;Article in Press.

[62] Chan C. Experimental Measurement of Effective Diffusion Coefficient of Gas Diffusion Layer/Microporous Layer in PEM fuel Cells. Master's thesis, University of Waterloo. 2011.

[63] Ocean Optics, Dunedin, FL. *NeoFox Installation and Operating Manual*. 2010.

[64] Kautsky H. Quenching of luminescence by oxygen. *Trans Farady Society*. 1939;35:216–219.

[65] Stubley G. ME663: Computational Fluid Dynamics. Course Material. 2011. Department of Mechanical and Mechatronics Engineering, University of Waterloo.

[66] Bird RB, Stewart WE, Lightfoot EN. *Transport Phenomena.* New York, NY: Wiley and Sons, 2nd ed. 2002.

[67] Kerkhof PJ, Geboers MA. Review: Analysis and extension of the theory of the theory of multicomponent fluid diffusion. *Chemical Engineering Science.* 2005;60:3129–3167.